Oceanic and continental lithospheric mantle in the 1.95 Ga Jormua Ophiolite Complex, Finland: implications for mantle and crustal evolution

Journal of Petrology

Valerie A. Finlayson
Department of Geology, University of Maryland, College Park MD, USA 27042

Mitchell Haller
Corning Inc, Corning NY, USA 14830

James M. D. Day
Scripps Institution of Oceanography, La Jolla CA, USA 92093

Stephen Ginley
Department of Earth and Environmental Sciences, University of Ottawa, Ottawa, Ontario, CAN, K1N 6N5

Brian O'Driscoll
Department of Earth and Environmental Sciences, University of Ottawa, Ottawa K1N 9A7, Canada

Asko Kontinen
Finland Geological Survey (GTK), Kuopio, FIN FI-7021

Eero Hanski
Oulu Mining School, 90014 University of Oulu, Finland

Richard J. Walker
Department of Geology, University of Maryland, College Park MD, USA 27042

ABSTRACT

The ca. 1.95 Ga Jormua Ophiolite Complex (JOC), Finland, is a rare Paleoproterozoic ophiolite that preserves a record of diverse upper mantle materials and melting processes. Meter-scale grid sampling of four JOC outcrops, as well as non-grid samples, permits evaluation of meter- to kilometer-scale mantle heterogeneity within the JOC. Significant heterogeneity is observed between the four grids, and also among a number of the non-grid samples examined. Variations in the concentrations of fluid-mobile elements are particularly large among different samples and locations. New whole-rock major, lithophile trace, and highly siderophile element data (HSE: Os, Ir, Ru, Pt, Pd, Re), including ^{187}Re-^{187}Os isotopic data, for serpentinized harzburgites indicate the presence of two distinct compositional types and probable modes of origin within the JOC. This is consistent with prior findings. Type 1 is similar to modern refractory abyssal-type mantle. Type 2 is more highly refractory than Type 1, and most likely represents samples from sub-continental lithospheric mantle (SCLM). Type 1 mantle is moderately heterogeneous with respect to chemical and Os isotopic compositions at both the meter and kilometer scales. By contrast, Type 2 mantle is considerably more homogeneous than Type 1 grids at the meter scale, but is more heterogeneous at the kilometer scale. The median initial γOs value for Type 1 mantle, calculated for 1.95 Ga, is ~-2.0 (where γOs is the % deviation in $^{187}Os/^{188}Os$ relative to a chondritic reference calculated for a specified time). This isotopic composition is consistent with a moderate, long-term decrease in Re/Os relative to the estimate for Primitive Mantle, prior to JOC formation. The similarity in this γOs value to the value for the modern abyssal mantle, as well as the initial values for several Phanerozoic ophiolites suggests that the upper mantle achieved a Re/Os ratio similar to the chondritic reference by ~2 Ga, then evolved along a subparallel trajectory to the chondritic reference since then. For this to occur, only limited Re

could have been permanently removed from the upper mantle since at least the time the JOC formed. A localized secondary metasomatic event at ~2 Ga, concurrent with the estimated obduction age for the JOC and subsequent Svecofennian Orogeny, affected the HSE systematics of some Type 1 samples. By contrast, late Archean Os T_{RD} model ages for Type 2 rocks indicate a depletion event superimposed upon the long-term Re depletion of the abyssal mantle. This event was established no later than ~2.6 Ga and may have occurred during a period of significant, well-documented crustal production in the Karelia craton at ~2.7 Ga.

INTRODUCTION

Documenting changes in the chemical composition of the upper mantle over time and the relationship of these changes to crustal formation is key to understanding the origin and evolution of important Earth processes, most notably plate tectonics. Chemical and isotopic characterization of the mantle portions of ophiolites provide one way to study changes in the upper mantle through time. Ophiolites are defined as crust-mantle assemblages of oceanic lithosphere, preserved in continental crust. Ophiolite sections include oceanic sediments, pillow basalts, sheeted dikes, gabbros, and mantle peridotites (e.g., Anonymous, 1972). It is normally assumed that the mantle and crustal lithospheric materials incorporated in ophiolites were formed either directly or indirectly from the convecting upper mantle within several tens of Myr before the obduction processes that led to their incorporation and preservation in stable continental crust (Dewey & Casey, 2011).

Ophiolites form along convergent margins and are often assigned an obduction age using the ages of cross-cutting igneous rocks and/or detrital zircons in associated metasedimentary rocks (e,g,. Peltonen et al., 1998; 2003). The majority of known ophiolites are Phanerozoic. Ophiolites in Proterozoic and Archean terranes are rare, underscoring their importance in preserving evidence for the development and progression of plate tectonic processes, including melt depletion of the convecting upper mantle, creation of oceanic lithosphere and eventual subduction of oceanic lithosphere (e.g., Kontinen, 1987; Helmstaedt & Scott, 1992: Scott et al., 1992; Stern et al., 1995; Peltonen et al., 1996, 1998, 2003, 2004; Şengör & Natal'in, 2004; Furnes et al., 2007; Kusky & Li, 2010; Kumar et al., 2010; Garde & Hollis, 2010; Dilek & Furnes, 2011; 2014; Furnes et al., 2014; Stepanova et al., 2014).

Ophiolite assemblages are typically highly altered as a result of processes associated with their obduction into stable continental settings. In particular, the ultramafic portions of ophiolite sequences commonly undergo variable degrees of serpentinization before, during and after obduction, although they may still retain some of their primary geochemical signatures (e.g., Deschamps et al., 2013; Malvoisin, 2015). The most noteworthy modifications concerns fluid-mobile element abundances (Day & Brown, 2021). Given the alteration history of such rocks, it is important to utilize geochemical tools capable of seeing through the effects of secondary modifications. Excluding gold, the highly siderophile elements (HSE: Re, Os, Ir, Ru, Rh, Pt, Pd, Au) have been shown to be resistant to certain secondary processes, such as serpentinization of mantle assemblages, while at the same time recording the timing and extent of primary mantle melting, and mantle metasomatic events (e.g., Snow et al., 2000; Pearson et al., 2003; Rudnick and Walker, 2009; Luguet and Pearson, 2019). It has also been shown that extraction of basaltic melts from the oceanic mantle has acted as a major control on the Re-Os isotopic evolution and relative abundances of HSE abundances in the residual convecting upper mantle (e.g., Walker et al., 2002; Pearson et al., 2003; 2004). Consequently, Os isotopes and HSE abundances in the mantle portions of ophiolites can potentially be used to place constraints on the volumes of prior oceanic crust removal and isolation from the upper mantle at various stages of Earth history (e.g., Walker et al., 2002; Walker, 2016).

Despite their importance, only a limited number of Precambrian ophiolites have been studied with respect to Os isotopes and the HSE. Kusky et al. (2007) reported Re-Os isotopic data for chromitites from the ~2.6 Ga Dongwanzi-Zunhua ophiolite, North China. All of the chromitites were characterized by very low Re/Os and initial $^{187}Os/^{188}Os$ consistent with chondritic reference growth models for the upper mantle. Walker et al. (1996) reported Re-Os

isotopic data for chromite, gersdorffite and laurite separates from chromitite hosted in the mantle section of the ~1.97 Ga Outokumpu ophiolite. That study found initial Os isotopic compositions that were broadly similar to a chondritic reference. By contrast, Tsuru et al. (2000) reported Re-Os isotopic data for chromitites and whole-rock mantle samples from the *ca*. 1.95 Ga Jormua Ophiolite Complex (JOC), Finland, and found that some chromitites and associated ultramafic whole-rock samples were characterized by having substantially subchondritic $^{187}Os/^{188}Os$ at the time of ophiolite formation, consistent with melt depletion of the rocks well before the ophiolite formed. Tsuru et al. (2000) concluded that at least a portion of the mantle materials sampled by the JOC consisted of sub-continental lithospheric mantle (SCLM) that had undergone melt depletion at ~3 Ga, preceding the obduction age by ~1 Gyr. Tsuru et al. (2000) also suggested that some portions of the JOC may represent a second, mid-ocean ridge basalt (MORB)-like subtype with generally chondritic initial $^{187}Os/^{188}Os$ for the time of ophiolite formation. Ancient MOR-like harzburgites preserved in the JOC, if confirmed, would represent a rare example of directly accessible ancient oceanic mantle material.

Here we re-investigate the JOC because of its importance for documenting the isotopic and chemical composition of upper mantle during the Proterozoic. We report whole-rock major, minor and lithophile trace element compositions, as well as HSE compositions and new Re-Os isotopic data for serpentinized peridotitic rocks. One major goal of this study is to constrain the melt depletion history of the portions of the mantle sampled by the JOC, prior to ophiolite formation, and re-examine the earlier conclusion of the presence of both MOR-like mantle and SCLM. A second goal is to attempt to link whole-rock analyses of HSE abundances and Os isotopic compositions with lithophile major and trace element compositions, in order to improve

130 understanding of the distribution and behavior of these elements in the upper mantle during the
131 Proterozoic.
132
133 **GEOLOGY**
134 The Jormua Ophiolite Complex is located in the central part of the N-S-trending Kainuu belt,
135 approximately 70 km from the southwestern margin of the Archean Karelia craton (**Figure 1**). In
136 addition, a chain of small ultramafic lenses of probable ophiolitic origin runs southward to the
137 Outokumpu area (south-southeast of the JOC) in the North Karelia belt (Peltonen, 2005; **Figure**
138 **1**), one of the Paleoproterozoic supracrustal belts in eastern and northern Finland (Laajoki,
139 2005). On both sides of the Kainuu belt, the Archean basement consists of gneissic and plutonic
140 tonalite-trondhjemite-granodiorite series rocks, and minor greenstone relics. Svecofennian (1.86-
141 1.80 Ga) granodiorite and granite plutons cut the Archean rocks and are particularly prevalent in
142 the area between the Kainuu belt and the Svecofennian arc complex. Broadly coeval with
143 emplacement of the JOC and granitoid intrusions, the Kainuu belt was also deformed and
144 metamorphosed during the 1.8–2.0 Ga Svecofennian Orogeny, with associated metamorphic
145 conditions reaching upper greenschist facies grade in the north, and amphibolite facies grade in
146 the south.
147 The JOC represents the most complete Paleoproterozoic ophiolitic sequence recognized,
148 covering an area of ~90 km^2 (**Figure 2**). In contrast to other Precambrian ophiolitic complexes
149 where crustal rocks dominate, e.g., the Payson Ophiolite, Arizona (Dann, 1997), approximately
150 half of the lithology of the JOC comprises rocks that were originally mantle peridotites (Peltonen
151 et al., 1996; 1998). Other rock types present in the JOC include gabbros, sheeted dikes, pillow
152 lavas, and minor pelagic sediments and plagiogranites (leucotonalite-trondhjemite). The mantle

153 rocks are cut by several generations of pyroxenitic and hornblenditic dikes (Peltonen et al.,
154 1998). A few small chromitite pods bearing primary chromite have been documented, while
155 disseminated chromites throughout the ophiolite are abundant, but mostly altered (Tsuru et al.,
156 2000). In these cases the original mineralogy is extensively replaced by secondary minerals,
157 although some chromites preserve primary cores. The ultramafic rocks mainly occur as
158 serpentinites, which have locally been further altered to talc-carbonate rocks and, in extreme
159 cases, to carbonate or quartz rocks (Peltonen et al., 1996; Säntti et al. 2006). A lower crustal
160 ultramafic-mafic cumulate series typical of Phanerozoic ophiolites (e.g., dunite transition zone,
161 or Moho transition zone; Boudier & Nicolas, 1995) is lacking, as sheeted dikes and gabbroic
162 bodies interleave with mantle rocks, sometimes separated by lens-like ultramafic septa. All
163 intrusive mafic rocks and pillow lavas appear to be co-magmatic, having been derived from the
164 same kind of enriched-mid ocean ridge basalt (E-MORB)-like parental magma (Peltonen et al.,
165 1996). The timing of the mafic magmatism in the JOC is constrained by precise U-Pb zircon
166 ages of 1952 ± 2 and 1950 ± 3 Ma obtained for a high-level gabbroic pod and trondhjemitic
167 differentiate, respectively (Huhma et al., 2018).

168 During its emplacement and the later Svecofennian-age orogeny, the JOC was
169 dismembered into four main tectonic blocks; the Hannusranta, Lehmivaara, Antinmäki, and
170 Kannas blocks (**Figure 2**). Of the four blocks, the Antinmäki block (also known as the Eastern
171 block; Peltonen et al., 1996; 1998) is the largest and best studied. It is the source of the majority
172 of samples reported in this study, including data for three grids (see below). The block consists
173 of serpentinized mantle peridotites and mantle-derived intrusive and extrusive rocks including
174 gabbros, Fe-gabbros, sheeted dikes and pillow basalts. A gabbroic dike that cross-cuts mantle
175 peridotite in this block yielded a U-Pb zircon age of 1953 ± 2 Ma (Peltonen et al., 1998); such

176 dikes are interpreted to represent feeder channels for gabbroic intrusions in the upper part of the
177 ophiolitic sequence.

178 The Lehmivaara (or Central) block also preserves serpentinized peridotite and dikes with
179 ocean island basalt-like (OIB) geochemical affinities, as well as sheeted dike complexes, all of
180 which were later cross-cut by E-MORB-like basalt dikes (Peltonen et al., 2003). Six
181 serpentinized peridotite samples from one grid were analyzed from this block.

182 The Hannusranta (or Western) block is composed almost totally of serpentinized
183 lherzolitic mantle rocks, with a paucity of E-MORB-like dikes and sheeted dikes (e.g., Peltonen
184 et al., 1996). A characteristic feature of the Hannusranta block is the presence of coarse-grained
185 clinopyroxene±amphibole and amphibole±garnet dikes and veins crystallized from an alkali
186 basalt magma at a depth of 30-50 km, which host Archean (xenocrystic) zircons (Peltonen et al.,
187 1998, 2003). No grid sampling was undertaken in the Hannusranta Block, however, two
188 individual harzburgitic samples from this block were analyzed. The Kannas block (also known as
189 the Northern block) was not sampled for this study, and so is not discussed further.
190

191 **SAMPLES**

192 Samples were collected either from drill cores or hand samples from bedrock exposures
193 (**Figure 3**; see **Table S1** for metadata). The majority of samples were collected during a field
194 campaign in 2015 (JU15 series), and the rest are whole-rock samples collected for and analyzed
195 by Tsuru et al. (2000) (samples with "ATK" designation).

196 While some samples reported here were collected as individual specimens from various
197 locations, samples from three 1.5 m × 1.5 m grids (Grid 1/JU15-16, Grid 2/JU15-18, and Grid
198 3/JU15-21), with nine subsamples from each grid, were collected from the Antinmäki block. Six

subsamples were collected from Grid 4 (JU15-25 to JU15-30) in the Lehmivaara block (**Figure 2**). All of the ultramafic rock sampled have undergone significant alteration, including serpentinization before peak regional metamorphism, which produced the present antigorite-dominated mineral assemblage. Consequently, hereafter we refer to the various petrologic groups by their presumed protoliths, based mainly on major element chemical compositions with particular emphasis on Mg#. The majority of the mantle rocks originated as harzburgites and dunites, and are the primary focus of this study. Comparison of geochemical variations on the ~0.5 m scale, versus variations in samples collected more than 1 km apart (**Figure 2**) is used to provide a metric for length scales of chemical and isotopic heterogeneity in the Paleoproterozoic mantle.

In total, we report whole-rock data for 53 samples from the JOC, with 41 collected from the Antinmäki block, 7 from the Lehmivaara block, and 7 from the Hannusranta block (**Figure 2**). Of these, 33 samples comprise the three complete and one partial grids, to assess meter-scale mantle heterogeneity. The 33 grid samples are the main focus of this study; ten non-grid harzburgite samples were analyzed to provide additional regional context (**Table S1; S3**). Several clinopyroxenite, hornblendite and plagiogranite samples were also collected and analyzed. Data for these rocks are provided in the **Electronic Supplement**.

ANALYTICAL METHODS

Sample Preparation

Samples were trimmed with a rock saw and polished with various grit sandpaper to remove tool marks. Pieces were then crushed in a ceramic jaw crusher and finely powdered in a ceramic

221 *Shatterbox*. Aliquots from the powders were used for all major, lithophile trace, and HSE
222 analyses, as well as Re-Os isotopic measurements.
223
224 **Major Elements**
225 Whole-rock major element data were obtained by X-ray fluorescence (XRF) analysis in two
226 campaigns: one in 2015 (Haller, 2017) and a second in 2019. Data were collected using a
227 *PANalytical Zetium* X-ray fluorescence vacuum spectrometer at Franklin and Marshall College,
228 Lancaster, PA, following methods described in Boyd & Mertzman (1987) and Mertzman (2000).
229 Loss on ignition (LOI) was determined by heating ~1 g sample powder at 950°C for approximately
230 90 minutes. The anhydrous sample powder was then mixed with lithium tetraborate, placed in a
231 platinum crucible, and heated with a Meker burner until molten, whereupon the material was
232 mixed for 10-12 minutes to ensure sample homogeneity. The molten sample was then quenched
233 in a Pt casting dish. Repeated analyses of BHVO-2 yielded accuracies of <1.5% for most major
234 elements (when comprising >0.5 wt.% of the anhydrous total). Minor elements (<0.5 wt.% of the
235 anhydrous total) and the alkaline oxides had an accuracy of <3%. The data were standardized after
236 methods outlined in Abbey (1983), Govindaraju (1994) and Mertzman (2000). The typical
237 reproducibilities (% 2σ) of the analyses were 0.8% for SiO_2, 1.3% for Al_2O_3, 2.3% for Fe_2O_3T,
238 1.0% for MgO, and 0.6% for CaO, based on repeated analyses of BHVO-2.
239
240 **Lithophile Trace Elements**
241 Lithophile trace element data for whole-rock samples were collected in three campaigns at the
242 Scripps Institution of Oceanography (SIO) using methods outlined in Day et al. (2014) and
243 O'Driscoll et al. (2015, 2018). The earlier set (2016) includes the JU15-16 (Grid 1) and JU15-18

(Grid 2) grid samples, while all the other samples were analyzed in campaigns in 2019 and 2022. All samples were analyzed along with basalt and peridotite rock standards (BHVO-2, BCR-2, BIR-1a, HARZ-01), as well as total procedural blanks. For these analyses, ~100 mg of sample powder was digested in a 1:4 mixture of concentrated high purity HNO_3:HF for >72 h at 150ºC on a hotplate. After drying down and sequential additional dissolutions and dry downs with HNO_3 to break down fluorides, clear sample solutions were obtained. These solutions were diluted by a factor of 5000 in 2% HNO_3 and doped with a 1 ppb In solution to monitor instrumental drift. Sample and standard solutions were measured in standard mode on a *Thermo Scientific iCAP Qc* quadrupole inductively-coupled plasma mass spectrometer (ICP-MS) at SIO. The reproducibility (2σ) of laboratory standards was <5% for the majority of elements compared to recommended values, where available (**Table S2**). Reproducibility of Cs, and to a lesser extent Cr, Li, and Ba was lower than for the majority of trace elements reported. Per-element internal statistics for standards are also provided in **Table S2**, in order to assess analytical reproducibility of elements across a representative range of concentrations.

Highly Siderophile Element Abundances and Re-Os Isotopes

Highly siderophile element concentrations and Re-Os isotopic system ratios were determined at the University of Maryland (UMd). Sample powders were digested using the Carius tube method described in Shirey & Walker (1995). Approximately 1.5 g of sample powder was loaded into each tube with known quantities of ^{185}Re-^{190}Os and HSE (^{191}Ir, ^{99}Ru, ^{194}Pt, ^{105}Pd) group spikes and ~4.5 mL of a 2:1 mixture of concentrated HNO_3 and concentrated HCl. Tubes were then sealed and heated for ~48 hours at ~260 ºC. Replicates and a harzburgite standard (MUH-1) were included in the analyses. After Carius tube digestion, samples were transferred to centrifuge

tubes pre-loaded with CCl_4 to extract Os from the sample solution. This extraction was repeated twice. Osmium was then back-extracted into concentrated HBr, dried down, and further purified using dichromate-HBr microdistillation. Sample Os separates were loaded onto Pt filaments along with a $Ba(OH)_2$ activator solution. Osmium abundances and isotopic compositions were analyzed using a *ThermoFisher Triton* multicollector mass spectrometer, using an ion counter in peak-hopping mode. The remaining HSE were separated using a primary AG-1x8 100-200 mesh anion resin column. The Re-Ru and, where necessary, Ir-Pt fractions were purified using scaled down versions of the primary chemistry. Abundances of Re, Ir, Ru, Pt and Pd were determined by isotope dilution using either a *Nu Plasma* or *ThermoFisher Neptune Plus* multi-collector inductively-coupled plasma mass spectrometer. Total analytical blanks (n= 9; 2016 and 2020 campaigns) were 0.4-2.9 pg Os, ≤12 pg Ir, 6.8-69 pg Ru, 97-432 pg Pt, 0.3-32 pg Pd and 0.6-13 pg Re. The average percent internal uncertainty on individual $^{187}Os/^{188}Os$ harzburgite analyses is ≤0.1 %2SE (**Table S4**; includes some data previously reported in Ginley, 2013; Haller, 2017). External reproducibility of $^{187}Os/^{188}Os$ of the UMCP Johnson-Matthey standard for the 2016 campaign was ±0.2 % 2σ (average 0.1137 ± 0.0002 2σ; n=17), and the 2019 campaign was ±0.1 % 2σ (average 0.1138 ± 0.0001 2σ; n=7).

RESULTS

Major and Lithophile Trace Element Abundances

Major and lithophile trace element compositions of 43 harzburgite and ten non-harzburgitic samples of various compositions are reported in **Tables 1** and **2**, respectively. Whole-rock major element compositions of harzburgites within each grid are characterized by only modest variations (**Figure 4A-F**). For example, within each grid, MgO typically varies by only ~2 wt.%.

There is no evidence for systematic correlations between MgO and Al_2O_3 among the samples (**Figure 4A**), as would be expected if the abundances of both elements were dominantly controlled by variable extents of partial melting (e.g., Herzberg, 2004; O'Driscoll et al., 2012). With respect to most major and minor elements, compositional variations within each grid are less than the compositional variations between the grids, where MgO varies, for example, by more than 5 wt.% (e.g., **Figure 4**). The compositions of individual (non-grid) samples vary considerably and cover nearly the entire range defined by collective samples from the four grids.

When normalized to primitive mantle (PM; Sun & McDonough, 1989), Pb concentrations are elevated in all grids except for Grid 3, with the greatest enrichments found in Grids 1 and 2 (**Figure 5**). Of the high field strength elements (HFSE), Th, Zr, Hf, and Ti are depleted in the majority of the harzburgites, while Nb and Ta are PM-like to slightly enriched. By contrast, Nb/U is more variable than Nb/Yb, but broadly elevated relative to PM throughout the sample suite (**Figure 6**).

Primitive mantle-normalized rare earth element (REE) patterns are highly variable among samples from the four grids (**Figure 7**). Samples from Grid 1 define relatively flat, but highly depleted patterns, whereas samples from Grids 2, 3 and 4 have higher overall abundances of REE than Grid 1, and are light REE (LREE) enriched. Patterns for Grid 2 samples are characterized by small positive Eu anomalies, while samples from Grids 3 and 4 show strong negative Eu anomalies (Eu/Eu* = 0.07-0.53; calculated as $Eu/Eu^* = Eu_N/sqrt(Sm_N*Gd_N)$ after Shields & Stille, 2001).

Highly Siderophile Element Abundances

312 Highly siderophile element compositions for JOC harzburgite samples vary substantially,
313 although most fall within the range of compositions defined by modern abyssal peridotites
314 (**Table 1; Figure 8A-D**). Most PM-normalized HSE patterns (PM values from Day et al., 2017)
315 are characterized by variable extents of depletion in the incompatible HSE Pd and Re. The
316 degree of HSE heterogeneity within a grid varies, with comparatively minor variability in Grids
317 3 and 4, and the greatest variability in Grids 1 and 2. The extent of heterogeneity among samples
318 from a grid is best assessed through the standard error of the whole-grid median concentrations
319 for each element (**Table 1**).

320 Grid 1 harzburgites are characterized by considerable variability in Ir, Ru, and Pd
321 compared to other grids (**Fig. 8A**). This grid has the strongest overall depletion (normalized to
322 PM, hereafter denoted by subscript "N") in Re_N/Ir_N of the samples analyzed, and Pd_N/Ir_N varies
323 from PM-like to strongly depleted (**Table 1**). While median Ir, Ru, and Pt concentrations (**Table**
324 **1**) in Grid 1 samples are similar to PM, individual samples within this grid show greater variation
325 compared to the other grids. Most samples also record depleted Os_N/Ir_N relative to PM, with the
326 lowest median ratio of all grids.

327 Most Grid 2 samples are characterized by relatively flat, PM-like abundances of Os
328 through Pt, but highly variable depletions in Pd (**Figure 8B**). Grid 2 patterns are more uniform
329 than Grid 1, although Pd and Pt are variably depleted. Sample JU15-18 C2 is an outlier with
330 pronounced Ru, Pt, and Pd depletions. Most samples from this grid have $Os_N/Ir_N < 1$, although
331 they are less strongly depleted than Grid 1. Unlike the other grids, most Grid 2 samples have
332 slightly elevated $Re_N/Ir_N \geq 1$, for all but one sample.

333 Grid 3 features relatively flat, PM-like HSE patterns in Os, Ir, and Ru, although several
334 samples are characterized by modest depletions in Ir (**Figure 8C**). Since Ir partitions similarly to

Os and to a lesser extent Ru, small depletions likely reflect involvement of phases that selectively incorporated Ir as well as Pt during depletion of some portions of JOC mantle (e.g. Pearson et al., 2004). By contrast, most samples from this grid are characterized by moderate depletions in Pt. Platinum can behave compatibly or incompatibly, depending on melting conditions, and for example, may be strongly fractionated in cratonic settings (Pearson et al., 2004). Palladium and especially Re are depleted in samples from this grid.

Grid 4 sample HSE patterns are characterized by remarkably uniform Os, Ir and Ru concentrations and very flat PM-normalized patterns (**Figure 8D**). Most Grid 4 patterns also have consistently depleted Pt and Pd concentrations relative to PM, with the exception of PM-like Pt and Pd in JU15-29. Most samples are characterized by strong depletions in Re. Samples JU15-27 and JU15-30, however, have more PM-like Re concentrations.

The non-grid harzburgite samples record localized minor enrichments or depletions in HSE relative to PM, with similar overall magnitudes of Re and Pd depletion relative to Ir (**Figure 8E**). Most of these samples have HSE patterns and a range of variation more closely resembling Grids 1 and 2, than Grids 3 and 4, most notably lacking the strong Pt depletion of Grids 3 and 4.

Rhenium-Osmium Isotopic Systematics

Initial $^{187}Os/^{188}Os$ is calculated for the presumed time of obduction at 1.95 Ga, (Peltonen et al., 1996), the assumed closure age of the Re-Os isotope system within the ophiolite, and helps to assess the potential for ancient melt depletion events predating the obduction age **(Table 2)**. Isotopic data for these rocks are also reported using the γOs_t notation, the percent deviation of the calculated $^{187}Os/^{188}Os$ of a sample relative to a chondritic reference at the time of interest. (see

Equation 1). The chondritic reference isotopic composition for 1.95 Ga is 0.11374, and $^{187}Re/^{188}Os_{chondrite}$ = 0.40186 using the parameters of Shirey and Walker (1998).

$$\gamma Os_t = 100 * \left(\frac{\frac{^{187}Os}{^{188}Os_{sample(t)}}}{\frac{^{187}Os}{^{188}Os_{chondrite(t)}}} - 1 \right) \qquad (1)$$

Harzburgites analyzed in this study have γOs_t values ranging from -10.7 to +8.3, with most values clustering between -5 and +2 (**Figure 10A**). The median value for all 43 harzburgites analyzed is -2.6 ± 0.7 (uncertainty reported throughout as 1SE of the median). The majority of samples from Grids 1 and 3 have relatively uniform, subchondritic γOs_t values that largely vary by only a few percent. Grid 1 has a median γOs_t of -2.1 ± 0.3 (n=9), while Grid 3 has the lowest median of the grids analyzed of -4.1 ± 0.4 (n=9). Variability (1SE of the median) of values for Grids 2 and 4 is considerably greater. Grid 2 has a median γOs_t of -0.2 ± 1.6 (n=9) that is similar to the chondritic reference. The greater variability may reflect the substantially higher $^{187}Re/^{188}Os$ ratios for samples from this grid compared to the others (~10×). This results in greater age corrections than for the lower Re/Os samples. Grid 4 is characterized by a γOs_t of -2.5 ± 1.9 (n=6). The two samples with the highest $^{187}Re/^{188}Os$ ratios have the most negative γOs_t values, suggestive of comparatively recent Re addition or Os loss. If they are removed from the median calculation, the remaining four samples are characterized by a γOs_t of -1.8 ± 1.0 (n=4).

Model Os melt extraction ages can be calculated using three methods: Mantle Extraction Ages (T_{MA}), Re-depletion Age type 1 (T_{RD1}) and Re-depletion Age type 2 (T_{RD2}) (Walker et al., 1989; McCoy-West et al., 2013; Rudnick & Walker, 2009; Luguet and Pearson, 2019). Details of these calculations are provided in the **Electronic Supplement**. These types of Os model ages are based on the assumption that the mantle material examined was affected by a single, significant melting event that removed some or even all Re from an originally fertile mantle peridotite

composition whose $^{187}Os/^{188}Os$ ratio had been previously evolving along an average chondritic growth trajectory. For both types of T_{RD} model age calculations it is assumed that Re was largely removed from the mantle sample examined during a single melting event. As true quantitative Re extraction is unlikely except for high degrees of partial melting (e.g., Handler et al., 1997), T_{RD} model ages are normally presumed to place *minimum* age constraints on the timing of melt depletion of the upper mantle. Importantly here, the model ages are calculated for both the present isotopic composition (T_{RD1}), and a projected initial isotopic composition using the measured $^{187}Re/^{188}Os$ (T_{RD2}). T_{MA} model ages, by contrast, are based on the assumption that the Re/Os of a peridotite has been maintained since the time of melt depletion. This type of model age calculation can be more accurate when partial melting, and therefore Re removal, was relatively modest. Secondary Re alteration as a function of melt-rock or water-rock interaction, however, becomes increasingly influential (and probable) in older rocks, resulting in over- or under-estimation of melting ages using the T_{MA}, for which growth trajectories are projected backward in time from the present measured $^{187}Re/^{188}Os$ to the chondritic evolution model.

All Os model age calculations require an assumption regarding the evolution of $^{187}Os/^{188}Os$ in the upper mantle. Choice of an evolutionary path is problematic for older rocks because Os isotopic data for upper mantle-derived rocks during the Proterozoic and Archean are rare. For this study, we utilized the parameters specified in Shirey and Walker (1998) in the model age calculations. These evolutionary parameters are broadly consistent with the evolution of the carbonaceous chondrite average, which by happenstance, appears to be broadly similar to the overall depletion history of the upper mantle, relative to estimates for the PM, which is more similar to the more radiogenic endmember compositions of ordinary and enstatite chondrites (e.g., Meisel et al., 2001; Walker 2016).

Median T_{MA} model ages for the four grids range from 2.2 to 2.8 Ga, exempting the two samples with high Re/Os (JU15-27 and JU15-30) from the calculation of the Grid 4 median. T_{RD1} model ages for grids 1, 3 and 4 range from 1.8 to 2.5 Ga. The majority of samples comprising these grids have significantly subchondritic $^{187}Re/^{188}Os$ (median <0.06; **Table 1**), consequently, most samples have similar T_{MA} and T_{RD1} model ages (**Figure 10C**).The median T_{RD1} model age calculation for Grid 2 gives a meaningless forward age of -0.5 Ga because the present-day $^{187}Os/^{188}Os$ ratios of most samples are higher than the chondritic reference. T_{RD2} model ages for all four grids range from 1.9 to 2.7 Ga. Again, because of the low Re/Os ratio for most samples from Grids 1, 3 and 4, T_{RD2} model ages are similar to their respective T_{MA} and T_{RD2} model ages. The median T_{RD2} for Grid 2 is broadly similar to the the T_{RD2} model age for Grid 1 (1.9 vs. 2.2 Ga) because the calculation takes into account the comparatively high Re/Os ratios of the Grid 2 samples.

Non-grid samples are characterized by highly variable model T_{MA}, T_{RD1} and T_{RD2} ages that range from 1.0 to 3.7 Ga, although some give impossibly old (ATK96) or forward ages (JU15-1) because they have $^{187}Re/^{188}Os$ ratios that are similar to or substantially greater than the chondritic reference (**Table 1; Figure 10B**).

DISCUSSION

Geochemical Evidence for Two Mantle Types in the JOC

Despite pervasive secondary alteration, numerous previous studies have identified ophiolite harzburgites as potential representatives of mantle that has undergone variable extents of melt depletion (e.g., Bernstein et al., 1998), as well as retaining broad characteristics suggestive of tectonic provenance. Consequently, several ophiolite subtypes have been identified, including

mid-ocean ridge (MOR), suprasubduction zone (SSZ), and continental margin (CM) types (e.g., Dilek and Furnes, 2011). Suprasubduction-type ophiolites are the most common, forming at convergent margins during trench rollback, and are interpreted to be associated with onset of major subduction-related geological events, such as ocean basin closure. Often, SSZ ophiolites preserve classical Penrose-type sequences, and sample highly melt-depleted, harzburgitic mantle. Volcanic sequences are typically MORB-like, arc-like, and/or boninitic (Dilek and Furnes, 2011, and references therein).

Mid-ocean ridge type ophiolites, like SSZ ophiolites, commonly display a Penrose structural sequence, but form in association with a MOR system, rather than solely a convergent margin. Geochemically, these ophiolites are associated with normal MORB (N-MORB) or E-MORB-like, with occasional examples of crustally contaminated MORB (C-MORB) present in the crustal portion of the ophiolite (Dilek and Furnes, 2011). Continental margin type ophiolites, which are associated with continental breakup and early stages of ocean basin opening, sample SCLM, which can lie in direct contact with overlying mafic igneous rocks, and may be cross-cut by dikes.

A major objective of this study is to reassess the tectonic provenance of different portions of the JOC, given that prior interpretations of JOC mantle lithologies have included E-MORB and ocean island basalt (OIB)-type source mantle (Peltonen et al., 1996), as well as SCLM (Tsuru et al., 2000; Peltonen and Kontinen, 2004). In the case of the confirmation of the presence of MOR-type mantle, compositional data can be used to improve constraints on the chemical and isotopic characteristics of abyssal mantle during the mid-Proterozoic. In the case of SCLM-type mantle, compositional and chronologic data can lead to an improved understanding of the nature

449 and timing of continental lithospheric mantle growth, and possible relationship to the evolution
450 of plate tectonics.

451 Chemical data alone cannot be used to distinguish MOR-type mantle from SCLM, as
452 both types of mantle have undergone variable extents of melt depletion. Some samples of SCLM
453 tend to show chemical evidence for more extreme melt depletion than is evidenced in abyssal
454 mantle, and for certain samples, SCLM tends to be characterized by greater levels of
455 metasomatic modification and/or re-melt enrichment than abyssal mantle (e.g., Zhang et al.,
456 2008). Although chemical composition fields defined by the global databases for each overlap
457 (**Figure 4**), possible distinguishing characteristics are present in trace elements. As examples,
458 serpentinized abyssal peridotites tend to have substantially greater Pb enrichment than SCLM,
459 perhaps related to the amount of seawater interacting with the two domains. Also, while SCLM
460 is often depleted in middle and heavy rare earth elements (MREE and HREE) compared to light
461 rare earth elements (LREE; e.g., Brenan et al., 1995; Li and Lee, 2006; Zhang et al., 2008;
462 Kodolányi et al., 2012), abyssal mantle is often LREE-depleted (**Figure 5-6**), although
463 metasomatized abyssal mantle may have LREE enrichment relative to MREE and HREE as a
464 result of fluid-rock interaction (Vander Auwera and Andre, 1991). Further, for some locales, Os
465 isotope model ages are a reliable indicator of the presence of SCLM, compared with abyssal
466 mantle, given that SCLM is commonly characterized by substantially older Os model ages than
467 abyssal mantle materials of the same presumed formation age. Hence, it was the Archean Os
468 model ages for some JOC peridotites that led Tsuru et al. (2000) to conclude that major portions
469 of the JOC represent SCLM that formed during the late Archean. As with prior studies, our new
470 data support the interpretation of two types of harzburgite in the JOC. Henceforth, they are
471 referred to as Type 1 and Type 2 mantle.

Type 1 Mantle (abyssal)

Type 1 mantle is characterized by comparatively low MgO (**Figure 4**), relatively unfractionated REE patterns, and HSE patterns consistent with moderate melt depletion, as evidenced by depletions in the incompatible HSE, Pd and Re, relative to PM (**Figure 8**). Type 1 as represented by Grids 1 and 2 is found mainly in the Antinmäki block, and represents most of the harzburgite samples in this study. The Al_2O_3 contents of Grids 1 and 2 are both strongly depleted, ranging between 1 to 2 wt.%. Grid 1 rocks have higher average MgO and lower average SiO_2 contents than Grid 2 (**Figure 4A-C**), consistent with a more refractory residue. Otherwise, the two grids have similar major element compositions.

Most trace element concentrations in Grid 1 samples, including the overall depletions in REE (~10× depletion relative to PM) and the minor LREE depletion relative to HREE are similar to modern abyssal lithospheric mantle (**Figures 5A, 6A**), as are the large positive Pb anomalies. Strong depletions in Pd are present in most Type 1 rocks, as well as especially strong Re depletions for all samples from this grid (**Figure 8A**). Osmium, Ir, Ru and Pt concentrations all show considerable variations within the grid, indicating processes in addition to simple melt removal, such as metasomatic overprinting.

Lithophile trace element patterns for Grid 2 are, as with Grid 1, broadly consistent with abyssal mantle (**Figure 5B**). Unlike Grid 1, however, Grid 2 samples are characterized by minor LREE enrichment and only minor HREE depletion, relative to PM (**Fig. 6A**). Rare earth element patterns of samples from this grid are similar to one another, indicating that the volume of material sampled was modified by a process that affected the REE in a uniform manner. In contrast to Grid 1 samples, Grid 2 samples are characterized by negligible Re depletion

compared to PM, but show a similar, broad range of Pd concentrations, which are moderately depleted relative to PM. These compositions suggest that Grid 2 mantle was initially melt-depleted, but that its Pd and Re budgets were subsequently modified. While Re can be fluid-mobile under oxidizing conditions (e.g., Xiong et al., 2006), co-occurrence of elevated Re (and Pd) with elevated LREE suggests that melt percolation probably controlled the re-enrichment of these elements. The retention of strong depletion in Al_2O_3, however, indicates that the effects of the putative melt-rock interaction was largely limited to incompatible trace elements. Importantly, melt percolation is also evidenced by the presence of pyroxenitic veins in the Grid 2 outcrop (**Figure 3**).

Additional information about the nature of the Type-1 mantle is revealed by HFSE systematics. As elements that are relatively insensitive to fractionation during partial melting and alteration, the relative abundances of Th, Nb, and Y can be used to evaluate the enrichment of both source mantle and mantle-derived melts (Pearce, 2008). Many of the JOC harzburgites, including Grid 2 samples, generally plot along the Th-Y-Nb mantle array, intermediate to modern N-MORB and E-MORB (**Figure 11**). Grid 1 samples, however, have Th abundances below the measurement detection limits (**Table 1**), and therefore, must plot well below the array. Given the highly incompatible nature of Th, its evident low abundances are likely associated with the process(es) that also led to the overall REE-depletion. Thorium mobility is unusual in metamorphic and subduction zone settings, but has been shown to occur along with U and REE loss (e.g., Ague, 2017), all of which are observed in Grid 1 samples.

Titanium and redox-sensitive V systematics (relative to Yb) provide constraints on the extent of melt depletion, depth of melting and oxidation state of a fertile MORB mantle (FMM) assumed to have a Primitive Mantle starting composition (Pearce & Parkinson, 1993). Modeled

518 compositional fields for enriched fertile (EFM) and refractory MORB mantle (RMM)
519 compositions are shown in **Figure 12**. Grid 1 and 2 samples plot as distinct clusters on the V and
520 Ti vs. Y plots. The differences in composition suggest kilometer-scale variability in depth and
521 fertility of the Type 1 protolith mantle. Grid 1 samples are more depleted in the incompatible
522 elements than Grid 2 samples, clustering near the RMM field, consistent with ~20% melt
523 extraction, slightly in excess of QFM redox conditions in the spinel-to-spinel+garnet stability
524 field. Grid 2 samples most closely resemble FMM, consistent with only 5-10% melt depletion,
525 and slightly favoring QFM to QFM-1 conditions that are more reduced than the other grids. The
526 minimal amount of melt extraction is unique to Grid 2, compared to the rest of the JOC. As noted
527 above, the protolith to Grid 2 samples appears to have been initially melt-depleted, and was
528 likely subjected to metasomatism that resulted in variable re-enrichment of portions of the grid.
529 All Grid 1 samples have low $^{187}Re/^{188}Os$ ratios <0.06, resulting in only minor age
530 corrections for γOs_t. All samples record modestly negative initial γOs_t values with a median
531 value of -2.0, similar to the median value for modern abyssal peridotites of -1.3 (Walker, 2016).
532 Given the low $^{187}Re/^{188}Os$ ratios for these samples, T_{MA}, T_{RD1} and T_{RD2} model ages are similar,
533 with median ages ranging only from 2.1 Ga (T_{RD1}) to 2.3 Ga (T_{MA} and T_{RD2}). Thus, model
534 depletion ages are older than the age of the ophiolite by only ~0.1 to 0.3 Gyr.
535 The Re-Os characterization of Grid 2 samples is more problematic, given the evidence
536 for the likely irregular, metasomatic addition of Re to the samples. The median initial γOs_t value
537 for this suite of -0.2 is significantly higher than for Grid 1, with greater variability among
538 individual samples (2σ of 1.6 and 7.5 for Grids 1 and 2, respectively). The respective median
539 T_{MA} and T_{RD2} ages of 2.2 and 1.9 Ga for this grid, however, are similar to ages for Grid 1, and
540 are consistent with melt depletion and subsequent metasomatic Re enrichment, soon after

ophiolite formation. The median T_{RD2} age is a meaningless future age because the $^{187}Re/^{188}Os$ of most samples are greater than the chondritic reference.

In summary, Os model ages for Grids 1 and 2 indicate melt depletion histories only shortly before the time of ophiolite formation. The HFSE suggest highly different degrees of partial melting are represented by Grids 1 (~20%) and 2 (<10%). Grid 1 melting occurred under comparatively oxidizing conditions between QFM and QFM+1 while Grid 2 melting occurring under somewhat less oxidizing conditions between QFM and QFM-1. Both grid suites appear to have been modified by secondary processes. In the case of Grid 1, both the low REE and Th abundances, and variability in incompatible HSE (Os, Ir and Ru) are evidence for likely metasomatic processes. In the case of Grid 2, LREE enrichment and variability in Pt concentrations are also indicative of metasomatic processes, albeit different from those that affected Grid 1. Overall, the chemical and especially Os isotopic characteristics of the Antinmäki block Grids 1 and 2 are most consistent with Paleoproterozoic abyssal lithospheric mantle.

Type 2 Mantle (SCLM)

Type 2 is represented by samples from Grids 3 and Grid 4. Grid 3 has both the highest MgO and Al_2O_3 (on an anhydrous basis) of the four grids, as well as the highest LOI and P_2O_5 contents (**Figure 4A, 4C**). Elevated volatiles and phosphate, while otherwise retaining major and trace element characteristics of harzburgite, may indicate secondary alteration involving carbonate-phosphate phases of the ultramafic protolith, such as has been described by Säntti et al. (2006). Secondary alteration is also consistent with a broader pattern of elevated LOI at high MgO contents in peridotites (see **Figure 4D** inset). Grid 4 samples, in contrast to Grid 3, are intermediate in various major element compositions to Type 1 Grids 1 and 2.

Lithophile trace element concentrations of both Grids 3 and 4 are more enriched than would be expected for refractory mantle, particularly considering that LREE abundances of the two grids are slightly enriched compared to PM, when LREE depletion is more typical in refractory compositions. This enrichment is distinct from LREE-enriched Grid 2 harzburgites (**Figures 5-6**). The sinusoidal REE patterns of Grids 3 and 4 feature convex, slightly enriched LREE (relative to PM), and concave, depleted MREE-HREE. The Type 2 REE patterns also feature well-developed negative Eu/Eu* anomalies that indicate that Type 2 mantle depletion occurred under more oxidizing conditions not present in Type 1 harzburgites.

Type 2 mantle is distinct from Type 1 in some, but not all, HFSE behavior (**Figures 11. 12**). In the Th-Yb-Nb plot (**Figure 11**), Grid 3 plots within the MORB-OIB mantle array, while Grid 4 samples plot below the mantle array. Unlike in the Type 1 case, Grid 4 Th and Yb abundances are comparable to Grid 3. Grid 4 samples, however, are more Nb-rich than Grid 3 (**Figures 5D, 7**), driving the shift away from the mantle array in **Figure 11**. Grid 3 and 4 samples exhibit evidence of 5 to 15% melt depletion along a Ti/Yb trajectory between the spinel and garnet stability fields (**Figure 12A**). This is also consistent with minor retention of HREE relative to MREE evident in Type 2 REE patterns, and is in contrast to Grids 1 and 2, which follow a Ti/Yb depletion trajectory consistent with melting in the spinel stability field. In the V-Yb diagram, Grids 3 and 4 plot in a scattered array with depletion levels consistent with variable Ti-Yb depletion (**Figure 12B**). The V-Yb data suggest that Grid 4 is slightly more depleted than Grid 3, and that both grids are considerably more oxidized than Type 1 harzburgites, with samples plotting in excess of QFM+1, consistent with the well-developed negative Eu anomalies in REE patterns for both grids.

586 The generally uniform HSE patterns for Grids 3 and 4 are depleted in Pt (**Figure 8**)
587 consistent with fractionation patterns observed in cratonic peridotites (Pearson et al., 2004), and
588 thus SCLM protoliths for Type 2 mantle. Some Grid 3 samples, where the most depleted γOs in
589 this study was found, also show depletions in Ir relative to Os and Ru. The uniformity and Pt±Ir
590 depletion found in the HSE patterns of the Type 2 grids are potentially controlled by a minor
591 phase not present in Type 1 mantle.
592 Grid 3 has a low $^{187}Re/^{188}Os$ median of 0.028, which, as with Grid 1, results in only
593 minor age corrections for calculating initial γOs_t values and model ages. Grid 3 has the most
594 strongly subchondritic median initial γOs_t value of -4.1, compared to the other JOC grids. This
595 median value is slightly higher than the average γOs_t value of -5.1 previously reported for JOC
596 chromites by Tsuru et al. (2000). As with Grid 1, the low $^{187}Re/^{188}Os$ ratios for these samples
597 result in similar T_{MA}, T_{RD1} and T_{RD2} model ages ranging from 2.5 Ga (T_{RD1}) to 2.7 Ga (T_{MA}).
598 Thus, the median model depletion ages for this grid is ~0.4 Gyr older than the median ages
599 determined for Grids 1 and 2 of the Type 1 harzburgites.
600 The median initial γOs_t value for Grid 4 of -2.5 is intermediate between the higher values
601 of Grids 1 and 2, and the lower value for Grid 3, albeit with considerable isotopic heterogeneity.
602 Two samples from this grid have $Re_N/Pd_N > 1$ and correspondingly high $^{187}Re/^{188}Os$, requiring
603 greater age correction than for the other grid samples, and these two samples (JU15-27 and
604 JU15-30) also have the lowest initial γOs_t values (-10.1 and -4.6, respectively). The scatter
605 among initial γOs_t values within the small area sampled, coupled with the presence of
606 pyroxenitic veins in the grid outcrop (see **Figure 3**) suggests that there may have been highly
607 localized (sub-meter scale) Re mobility at the sample site, sufficiently long after the main Re
608 depletion event that single-stage age correction may not fully account for ^{187}Os ingrowth.

609 Nevertheless, median T_{MA} and T_{RD2} model ages are in good agreement at 2.5 Ga and similar to
610 Grid 3.
611
612 *Non-Grid Samples*
613 The non-grid samples represent a mixture of Type 1, including both LREE-enriched and depleted
614 examples, and Type 2 harzburgite (see **Table 2** for list of samples by category), distinguished
615 mainly by trace element characteristics (REE patterns, Eu/Eu*, and to a lesser extent, degree of
616 Pb enrichment). Type 1 LREE-enriched are the most common non-grid harzburgite type (n=5).
617 Extended trace element patterns have large positive Pb anomalies (~10x Ce), and nearly PM-
618 like, slightly LREE-enriched REE patterns with minor positive to negative Eu/Eu* anomalies,
619 closely resembling Grid 2 (**Figures 5-6**). Two of the non-grid harzburgites considered to be Type
620 1 are more similar to Grid 1 samples, with large positive Pb anomalies (**Figure 5**), and LREE
621 depleted patterns. Collectively, all of the non-grid Type 1 samples have T_{RD2} ages ranging from
622 1.6-2.4 Ga, with a median value of 1.9 Ga, and γOs_t values ranging from -10.7 to +1.8, with a
623 median of +0.5. These samples are overall more radiogenic than Grid 1, more closely resembling
624 Grid 2.
625 Three of the non-grid harzburgites belong to Type 2 (resembling Grids 3 and 4). For
626 these samples, Pb enrichment is more muted (resembling Grid 4) than the other non-grid
627 harzburgites, and while REE abundances vary, pattern shapes resemble the sinusoidal Grid 3 and
628 4 patterns, with well-developed negative Eu/Eu*. Unlike with the grid samples, the non-grid
629 Type 2 samples only show small Pt depletions (**Figure 13A**). Two of the samples (ATK59 and
630 ATK589) have negative γOs_t (both yielding values of -2.7) that give identical T_{RD2} ages of 2.4
631 Ga, which closely resemble Re-Os systematics of Grid 4 (median γOs_t of -2.5, and T_{RD2} of 2.4

632 Ga). The third sample (JU15-1) has high $^{187}Re/^{188}Os$ and was duplicated. Like most other
633 samples reported here, the three model ages disagree for both replicates, and overall the sample
634 replicated poorly (T_{RD2} of 2.4 Ga and 4.6 Ga for the duplicates; the first of which is identical to
635 ATK59 and ATK589). Based on the elevated Re concentration and more radiogenic Os, the
636 duplicate analysis may have included a small amount of material that had been subjected to Re
637 contamination significantly later than obduction, and its calculated initial $^{187}Os/^{188}Os$ should be
638 discounted.
639 In summary, incompatible lithophile trace elements are more fractionated from PM
640 values in rocks from Grids 3 and 4 compared to the rocks of Grids 1 and 2, e.g., LREE
641 enrichment and strong negative Eu anomalies. They also show evidence for having formed or
642 been modified in a more oxidizing environment. Highly siderophile element patterns, however,
643 are indistinguishable from modern abyssal peridotites. Despite this, both Grids 3 and 4 are
644 characterized by T_{MA} and T_{RD2} model ages that are ~400-500 Myr older than ophiolite formation.
645 We conclude that these grid locales in the Antinmäki and Lehmivaara blocks sample SCLM that
646 likely formed, at latest, at the end of the Archean.
647
648 **Mantle Heterogeneity in the JOC**
649 Overall, geochemical variability in the JOC at the meter scale is similar to that at the kilometer
650 scale within the Type 1 harzburgites (Grids 1 and 2). By contrast, Type 2 grids (Grids 3 and 4)
651 have distinctive, more uniform HSE behavior at the meter scale, suggesting that their protolith
652 mantle was more homogeneous than Type 1 mantle. Most of the variance in Type 2 harzburgites
653 is outlier-controlled, indicative of highly localized heterogeneities. Type 1 mantle is more
654 common than Type 2 mantle harzburgites in our sample set, although this sampling is not

655 statistically representative of the mantle in the JOC. The new data, however, lend some insight to
656 the distribution of abyssal and SCLM domains within the JOC (**Figure 2**).
657 Within the Antinmäki Block, which is the best-characterized JOC block, both Type 1 and
658 2 harzburgites are present. Type 2 mantle is found in the central-western, northeastern, and
659 southeastern margins of the lherzolitic portion of the block; all are separated by at least 2 km.
660 Two of these sites are located within several tens to hundreds of meters of Type 1 harzburgites.
661 In both of these examples, LREE-enriched Type 1 harzburgites (e.g., resembling Grid 2) occur
662 near Type 2 domains. The LREE-depleted Type 1 harzburgites (resembling Grid 1) described in
663 this study are all from the southeast corner of the Antinmäki Block and sit further from known
664 outcrops of the Type 2 domain. The transition between LREE-enriched Type 1 mantle and Type
665 2 mantle appears to be abrupt, occurring within tens to hundreds of meters.
666 The harzburgites from the Lehmivaara and Hannusranta Blocks are all Type 2 mantle, but
667 represent only limited sampling of both blocks compared to the Antinmäki samples. Hence,
668 additional characterization of rocks from these blocks will be necessary to more meaningfully
669 assess the distributions of mantle type.
670 The juxtaposition of Type 1 and Type 2 mantle within the ophiolite may be explained as
671 a function of the tectonic history of the Kainuu belt, which hosts the JOC and related ophiolitic
672 and ultramafic complexes. Prior studies interpreted the JOC as a "passive margin" ophiolite
673 (Kontinen, 1987; Peltonen et al., 1996; 1998), where lithologies would be expected to transition
674 between those characteristic of the oceanic versus continental (or cratonic) lithosphere, hence
675 accounting for the presence of both mantle types throughout the JOC. After being "detached"
676 from the ocean basin during early stages of continental breakup, the JOC was likely
677 dismembered during the initial thrusting onto the margin of the Karelian craton (Peltonen and

678 Kontinen, 2004). The presence of Type 1 mantle in a Paleoproterozoic ophiolite provides a rare
679 opportunity to examine the Os isotopic compositon of a portion of the ancient DMM.
680
681 **Osmium isotopic composition of the abyssal mantle during the Proterozoic**
682 Tsuru et al. (2000) reported a γOs_t value of ~-5.1 for what is defined here as Type 2 JOC mantle.
683 This is ~1 % lower than the estimate of ~-4 reported here for Grid 3. The value reported by
684 Tsuru et al. (2000) was largely based on data for chromitites and chromites separated from
685 serpentinites (originally harzburgites). Tsuru et al. (2000) also analyzed whole-rock serpentinites
686 from which the chromites were separated, averaging a value of γOs_t of ~-4 that is virtually
687 identical to the Grid 3 median value. The difference in isotopic compositions between chromite
688 and whole rock is puzzling. Chromite was originally viewed as the ideal recorder of mantle Os
689 isotopic composition in ophiolite peridotites because of the high abundance of Os and low Re/Os
690 typical of such chromites (e.g., Walker et al., 2002). It has been subsequently been argued,
691 however, that chromite present in mantle assemblages are more likely to concentrate Os that is
692 *more* radiogenic than is representative of the mantle domain within which it forms (O'Driscoll et
693 al., 2012; 2015). This is because the Os that is concentrated is most likely derived from
694 intergrain sulfides, which have been shown to have higher Re/Os than the bulk rock in which
695 they originally resided and thus, become more radiogenic (Alard et al., 2005). The offset
696 between the previously reported chromitite compositions in Type 2 JOC and whole-rock
697 analyses cannot be easily explained and highlights the likelihood that the average model
698 depletion age for the bulk samples here may serve as only minimum ages, and that the creation
699 of the SCLM may have predated the average model age by several 100 Myr.

Tsuru et al. (2000) proposed that MORB-like (abyssal) mantle was also present in the JOC. This observation is confirmed here in the presence of Type 1 rocks. Our new data show that at least part of the Type 1 mantle (LREE-depleted; e.g., Grid 1) records the time-integrated removal of Re from the upper mantle, relative to the PM, that may have begun during early Earth history, perhaps related to one or more episodes of significant crustal growth (e.g., Pearson et al., 2007). Examples of Type 1 LREE-enriched mantle (e.g., Grid 2; **Table 2**) shows evidence of later metasomatic overprinting and Re addition not typical of the LREE-depleted group, which resulted in considerable scatter in the Os isotopic composition of these samples compared to Type 1 LREE-depleted and Type 2 samples (**Figure 10**). Despite the scatter, the median γOs_t for all Type 1 LREE-enriched samples (+0.2 ± 1.3) is indistinguishable from the chondritic reference, consistent with Re mobility concurrent with JOC obduction. Whether or not the Type 1 LREE-enriched samples are a faithful record of Os isotopic compositions in the DMM at 1.95 Ga, or partially a record of metasomatic processes, merits further study.

Considering only Type 1 samples with good agreement between T_{MA}, T_{RD1}, and T_{RD2} model Re depletion ages (**Figure 10**, e.g. within variance of 0.3 Ga, after Rudnick & Walker, 2009), Type 1 mantle has a median γOs_t of -2.1 ± 0.9. Including all Type 1 samples shifts the median γOs_t only slightly to -2.0 ± 0.8, suggesting the median estimate is robust to outliers. This median value is nearly identical to the Snow and Reisberg (1995) estimate for modern DMM of -1.9 ± 1.1 based on unaltered examples of modern abyssal peridotite. Subsequent estimates of γOs for the modern DMM, using much larger datasets, have minimally changed this estimate, with γOs values ranging only from -2.0 (Lassiter et al., 2014) to -1.3 (Walker, 2016). Assuming JOC Type 1 mantle is representative of DMM at 1.95 Ga, the JOC median suggests that the offset of

722 the Os isotopic composition of early Proterozoic DMM relative to the chondritic reference is
723 nearly identical to that for the modern DMM (**Figure 14**).

724 Secular and/or spatial changes in the Os isotopic composition of the DMM are apparent
725 when considering a global and temporal distribution of harzburgite and chromite samples from
726 ophiolite complexes that have been previously characterized for Re-Os isotopic systematics
727 (**Figure 14; Table 3**). Median γOs_t values are determined from samples not significantly
728 affected by high Re abundance ($Re_N/Pd_N > 1$). The median Os isotopic composition of Type 1
729 JOC mantle ($\gamma Os = -2.0$) resembles that of many modern ophiolites in addition to the Snow &
730 Reisberg (1995) estimate ($\gamma Os = -1.9$) for modern DMM. Given that negative γOs values in
731 abyssal mantle, relative to the chondritic reference and PM, at the time of obduction is assumed
732 to reflect prior Re removal (via melt extraction) from the source, at least part of the JOC Type 1
733 mantle must have been depleted in Re no later than the early Proterozoic (e.g., Grid 1).

734 In a simple model of progressive extraction of crust (Re) from abyssal mantle over time,
735 abyssal mantle would be expected to evolve to Os isotopic compositions that increasingly grows
736 to less radiogenic compositions than the evolution trajectory of the PM. Although the availability
737 of Os isotopic data for samples of abyssal mantle through time are limited, most ophiolites
738 appear to show some level of long-term Re depletion relative to PM (**Fig. 14**). The γOs_t value of
739 the abyssal mantle portion of the JOC of -2.0 is noteworthy in that it is similar to the value for
740 the modern DMM. If representative of the DMM, this suggests that the level of Re depletion in it
741 was nearly complete by ~2.0 Ga, and that the Os isotopic composition of the DMM has evolved
742 along a trajectory that is parallel to the chondritic reference of Shirey and Walker (1998). This in
743 turn suggests the $^{187}Re/^{188}Os$ of the DMM has been nearly identical to the chondritic reference
744 ratio of 0.402 (Shirey and Walker, 1998), indicating that significant Re extraction had occurred

745 by the early Proterozoic in at least some portions of the upper mantle reservoir, providing some
746 of the earliest whole-rock evidence of ancient melt extraction.

747 Unlike peridotites from most younger, similarly well-documented ophiolites, the majority
748 of JOC harzburgites have Re-Os model ages that predate obduction. Model ages for three of the
749 four grid samples further demonstrate good internal agreement. By contrast, only sparse
750 examples of similarly ancient Re depletion remains in the modern upper mantle, largely confined
751 to single chromites, sulfides, and/or Os-Ir alloys (e.g., Harvey et al., 2006; Liu et al., 2022),
752 although some rare examples of ancient melt events have been found in modern whole-rock
753 abyssal peridotite samples (Liu et al., 2008). These isolated examples from Phanerozoic
754 peridotites tend to reproduce poorly, which is often attributed to heterogeneous Os-Ir-rich phases
755 hosted in mantle rocks. It is possible that the whole-rock "memory" of ancient crustal building
756 was erased from the convecting upper mantle as a function of crustal recycling and younger
757 crustal building events between the early Proterozoic and modern mantle, as suggested by Meisel
758 et al. (2001). Further, the budgets of isolated recycled crust may not be constant, or
759 homogenously distributed over the temporal and spatial extent of the upper mantle, evidenced by
760 the apparent shift in median Os isotopic composition of the DMM towards higher γOs values,
761 implying higher Re/Os, in late Proterozoic to early Cambrian ophiolites before returning to lower
762 Re/Os and a γOs value more like modern DMM (**Figure 14**; e.g., Haller et al., 2021; Paquet et
763 al., 2022). While the spatial extent and contributions of fertile and depleted DMM domains
764 through time remains ambiguous, the new JOC data, combined with information from younger
765 ophiolites, reveals potential secular changes in the Os isotopic composition of the DMM. Thus,
766 the Re-Os isotopic record of Type 1 JOC mantle confirms findings of ancient Re depletion, and

767 together with the record obtained from younger ophiolites, suggests that siderophile cycling in
768 the convecting mantle may be more complex and dynamic than previously thought.
769
770 **CONCLUSIONS**
771 The 1.95 Ga Jormua Ophiolite Complex, one of the oldest known complete ophiolite sequences,
772 preserves a heterogeneous mixture of serpentinized mantle domains, likely consisting of both
773 abyssal- and SCLM-type mantle and associated mantle-derived melts. The harzburgites
774 examined herein have refractory major element, HSE and Re-Os systematics consistent with a
775 major mantle melting event that affected the majority of the protolith mantle that occurred at a
776 minimum age of ~2.6-2.5 Ga, placing the formation of the majority of the mantle material in the
777 JOC at the Archean-Proterozoic transition. We further identify the presence of abyssal
778 harzburgite that existed no later than the Archean-Proterozoic transition, making the JOC a host
779 of rarely-preserved ancient oceanic mantle material in addition to previously documented
780 Archean SCLM.
781 Localized evidence of a second melting event ~2 Ga is present in a minor portion of the
782 samples characterized in this study, consistent with prior age determinations for mantle dikes that
783 cross-cut portions of the ophiolite, related to the obduction process and following Svecofennian
784 orogeny and regional metamorphism. Trace element systematics indicate widespread, but highly
785 variable, melt-rock and fluid-rock re-enrichment processes, which is also reflected as elevated Re
786 in some of the harzburgite samples.
787 Grid sampling records HSE compositions more uniform at the meter scale than at the
788 kilometer scale in three of the four grid sites within the JOC. The exception is Grid 1, which also
789 records the least re-enrichment of the grid sites; most other locales exhibit highly localized (sub-

meter scale) evidence of likely melt-rock interaction that re-enriched REE budgets and possibly Re. Overall, length-scale variations best resemble those found in the 161 Ma Coast Range Ophiolite in California, but contrast with the 497 Leka and 492 Ma Shetland ophiolites, which have better developed meter-scale heterogeneities and evidence of less extensive melt depletion.

The presence of Type 1 (abyssal) mantle in the JOC provides an estimate of the DMM at ~1.95 Ga, showing that at least some portion of the Paleoproterozoic upper mantle was depleted relative to a chondritic reference. Compared to modern DMM sampled by younger ophiolites, JOC abyssal mantle underwent a similar extent of depletion. By contrast, a cluster of ophiolites formed during and immediately following the Proterozoic-Cambrian transition are less melt-depleted, resembling a chondritic reference, suggesting that the osmium isotopic composition of the DMM is heterogeneous throughout its history or underwent long-term compositional shifts related to depletion and re-enrichment, or a combination of the two.

ACKNOWLEDGEMENTS

The Geological Survey of Finland/GTK is commended for supporting field work of A.K. Jairus Slagle provided invaluable assistance processing samples for analytical work. The authors acknowledge NSF Petrology and Geochemistry grant #1423879 to R.J.W. B.O'D. acknowledges support from a Royal Society Research Grant (RG100528) and from Natural Environment Research Council (NERC) grant NE/J00457X/1. JD acknowledges NSF petrology and geochemistry grant NSF EAR 1447130.

DATA AVAILABILITY

The data reported in this article are available in this article and in its supplementary material.

813
814
815
816

REFERENCES

Abbey, S. (1983). Studies In" standard samples" of silicate rocks and minerals 1969-1982. *Geological Survey of Canada, Paper 114*, 83-15.

Agranier, A., Lee, C. T. A., Li, Z. X. A. & Leeman, W. P. (2007). Fluid-mobile element budgets in serpentinized oceanic lithospheric mantle: insights from B, As, Li, Pb, PGEs and Os isotopes in the Feather River Ophiolite, California. *Chemical Geology 245*(3-4), 230-241. 10.1016/j.chemgeo.2007.08.008

Ague, J. J. (2017). Element mobility during regional metamorphism in crustal and subduction zone environments with a focus on the rare earth elements (REE). *American Mineralogist* 102(9), 1796–1821. Doi:10.2138/am-2017-6130

Alard, O., Luguet, A., Pearson, N. J., Griffen, W. L., Lorand, J.-P., Gannoun, A., Burton, K. W. & O'Reilly, S. Y. (2005) In situ Os isotopes in abyssal peridotites bridge the isotopic gap between MORBs and their source mantle. *Nature* 436, 1005-1008.

Anonymous. (1972). Penrose field conference on ophiolites. *Geotimes*, *17*(12), 24-25.

Bernstein, S., Kelemen, P. B. & Brooks, C. K. (1998). Depleted spinel harzburgite xenoliths in Tertiary dykes from East Greenland: restites from high degree melting. *Earth and Planetary Science Letters 154*(1-4), 221-235.

Boudier, F. & Nicolas, A. (1995). Nature of the Moho transition zone in the Oman Ophiolite. *Journal of Petrology* 36, 777-796.

Boyd, F. R. & Mertzman, S. A. (1987). Composition and structure of the Kaapvaal lithosphere, southern Africa. In: B. O. Mysen (ed.) *Magmatic Processes: Physicochemical Principles*. Geochemical Society, Special Publication *1*, 3-12.

Brenan, J., Shaw, H. & Ryerson, F. (1995). Experimental evidence for the origin of lead enrichment in convergent-margin magmas. *Nature* 378, 54–56. https://doi.org/10.1038/378054a0

Büchl, A., Brügmann, G., Batanova, V. G., Münker, C. & Hofmann, A. W. (2002). Melt percolation monitored by Os isotopes and HSE abundances: a case study from the mantle section of the Troodos Ophiolite. *Earth and Planetary Science Letters 204*(3-4), 385-402. DOI:10.1016/S0012-821X(02)00977-9

Dann, J. C. (1997). Pseudostratigraphy and origin of the Early Proterozoic Payson ophiolite, central Arizona. *Geological Society of America Bulletin* 109 (3), 347–365.

Day, J. M. D., Peters, B. J. & Janney, P. E. (2014). Oxygen isotope systematics of South African olivine melilitites and implications for HIMU mantle reservoirs. *Lithos 202*, 76-84. https://doi.org/10.1016/j.lithos.2014.05.009

Day, J. M. D., Walker, R. J. & Warren, J. M. (2017). ^{186}Os–^{187}Os and highly siderophile element abundance systematics of the mantle revealed by abyssal peridotites and Os-rich alloys. *Geochimica et Cosmochimica Acta 200*, 232-254. https://doi.org/10.1016/j.gca.2016.12.013

Day, J. M. D. & Brown, D. B. (2021). Ancient melt-depletion in fresh to strongly serpentinized Tonga Trench peridotites. *Journal of Petrology* 62, egab088, https://doi.org/10.1093/petrology/egab088

Deschamps, F., Godard, M., Guillot, S. & Hattori, K. (2013). Geochemistry of subduction zone serpentinites: A review. *Lithos 178*, 96-127. https://doi.org/10.1016/j.lithos.2013.05.019

Dewey, J. F. & Casey, J. F. (2011). The origin of obducted large-slab ophiolite complexes. In: *Arc-Continent Collision*. Springer, Berlin, Heidelberg, pp. 431-444

Dilek, Y. & Furnes, H. (2011). Ophiolite genesis and global tectonics: geochemical and tectonic fingerprinting of ancient oceanic lithosphere. *Geological Society of America Bulletin 123*, 387–411. https://doi.org/10.1130/B30446.1

Dilek, Y. & Furnes, H. (2014). Ophiolites and their origins. *Elements* 10, 93–100. https://doi.org/10.2113/gselements.10.2.93

Frei, R., Gervilla, F., Meibom, A., Proenza, J. A. & Garrido, C. J. (2006). Os isotope heterogeneity of the upper mantle: Evidence from the Mayari–Baracoa ophiolite belt in eastern Cuba. *Earth and Planetary Science Letters 241*(3-4), 466-476. https://doi.org/10.1016/j.epsl.2005.11.043

Furnes, H., de Wit, M., Staudigel, H., Rosing, M. & Muehlenbachs, K. (2007). A vestige of Earth's oldest ophiolite. *Science 315*(5819), 1704-1707. DOI: 10.1126/science.1139170

Furnes, H., De Wit, M. & Dilek, Y. (2014). Four billion years of ophiolites reveal secular trends in oceanic crust formation. *Geoscience Frontiers 5*(4), 571-603. https://doi.org/10.1016/j.gsf.2014.02.002

Garde, A. A. & Hollis, J. A. (2010). A buried Palaeoproterozoic spreading ridge in the northern Nagssugtoqidian orogen, West Greenland. *Geological Society, London, Special Publications 338*(1), 213-234. DOI:10.1144/SP338.11

Ginley, S. (2013). Geochemical history of the convecting upper mantle: A comparison of ophiolites. BSc Thesis, University of Maryland, College Park.

Gong, X. H., Xu, J. F., Liu, X. J., Huang, X. X., Zhang, Z. G., Zhou, H. L., Yang, Z. Y. & Zhao, W. X. (2020). Widespread Os-isotopically ultradepleted mantle domains in the Paleo-Asian oceanic upper mantle: evidence from the Paleozoic Tianshan ophiolites (NW China). *International Journal of Earth Sciences 109*(4), 1421-1438.

González-Jiménez, J. M., Barra, F., Walker, R. J., Reich, M. & Gervilla, F. (2014). Geodynamic implications of ophiolitic chromitites in the La Cabaña ultramafic bodies, Central Chile. *International Geology Review 56*(12), 1466-1483. DOI:10.1080/00206814.2014.947334

Govindaraju, K. (1994). 1994 compilation of working values and sample description for 383 geostandards. *Geostandards Newsletter 18*, 1-158. https://doi.org/10.1046/j.1365-2494.1998.53202081.x-i1

Haller, M. B. (2017). Meter-scale heterogeneities in the oceanic mantle revealed in ophiolite peridotites, MSc Thesis, University of Maryland, College Park.

Haller, M. B., O'Driscoll, B., Day, J. M. D., Daly, J. S., Piccoli, P. M. & Walker, R. J. (2021). Meter-scale chemical and isotopic heterogeneities in the oceanic mantle, Leka ophiolite complex, Norway. *Journal of Petrology 62*(12), egab061 https://doi.org/10.1093/petrology/egab061

Handler, M. R., Bennett, V. C. & Esat, T. M. (1997). The persistence of off-cratonic lithospheric mantle: Os isotopic systematics of variably metasomatised southeast Australian xenoliths. *Earth and Planetary Science Letters 151*(1-2), 61-75. https://doi.org/10.1016/S0012-821X(97)00118-0

Harvey, J., Gannoun, A., Burton, K. W., Rogers, N. W., Alard, O. & Parkinson, I. J. (2006). Ancient melt extraction from the oceanic upper mantle revealed by Re–Os isotopes in abyssal peridotites from the Mid-Atlantic ridge. *Earth and Planetary Science Letters 244*(3-4), 606-621. https://doi.org/10.1016/j.epsl.2006.02.031

907 Helmstaedt, H. H. & Scott, D. J. (1992). The Proterozoic ophiolite problem. In: Condie, K. C.
908 (ed.) Proterozoic Crustal Evolution. *Developments in Precambrian Geology* 10, . Elsevier,
909 Amsterdam, pp. 55-95.
910 Herzberg, C. (2004). Geodynamic information in peridotite petrology. *Journal of*
911 *Petrology 45*(12), 2507-2530. https://doi.org/10.1093/petrology/egh039
912 Huhma, H., Hanski, E., Kontinen, A., Vuollo, J., Mänttäri, I. & Lahaye, Y. (2018). Sm-Nd and
913 U-Pb isotope geochemistry of the Palaeoproterozoic mafic magmatism in eastern and
914 northern Finland. *Geological Survey of Finland, Bulletin* 405, 150 p.
915 Kodolányi, J., Pettke, T., Spandler, C., Kamber, B. S. & Gméling, K. (2012). Geochemistry of
916 ocean floor and fore-arc serpentinites: constraints on the ultramafic input to subduction
917 zones. *Journal of Petrology 53*(2), 235-270. https://doi.org/10.1093/petrology/egr058
918 Kontinen, A. (1987). An early Proterozoic ophiolite—the Jormua mafic-ultramafic complex,
919 northeastern Finland. *Precambrian Research 35*, 313-341. https://doi.org/10.1016/0301-
920 9268(87)90061-1
921 Kontinen, A. (1998). Geological Map of the Jormua area. 1:50 000. *Geological Survey of*
922 *Finland, Special Paper* 26, Appendix 2.
923 Kumar, K. V., Ernst, W. G., Leelanandam, C., Wooden, J. L. & Grove, M. J. (2010). First
924 Paleoproterozoic ophiolite from Gondwana: geochronologic–geochemical documentation of
925 ancient oceanic crust from Kandra, SE India. *Tectonophysics 487*(1-4), 22-32.
926 https://doi.org/10.1016/j.tecto.2010.03.005
927 Kusky, T. M., Li, J. H. & Tucker, R. D. (2001). The Archean Dongwanzi ophiolite complex,
928 North China Craton: 2.505-billion-year-old oceanic crust and mantle. *Science 292*(5519),
929 1142-1145. DOI: 10.1126/science.1059426
930 Kusky, T. M. & Li, J. H. (2002). Is the Dongwanzi complex an Archean ophiolite?
931 Response. *Science 295*(5557). doi:10.1126/science.295.5557.923a
932 Kusky, T. M., Zhi, X., Li, J., Xia, Q., Raharimahefa, T. & Huang, X. (2007). Chondritic osmium
933 isotopic composition of Archean ophiolitic mantle, North China craton. *Gondwana*
934 *Research 12*(1-2), 67-76. https://doi.org/10.1016/j.gr.2006.10.023
935 Kusky, T. M. & Li, J. (2010). Origin and emplacement of Archean ophiolites of the central
936 orogenic belt, North China craton. *Journal of Earth Science 21*(5), 744-781.
937 https://doi.org/10.1016/S0166-2635(04)13007-7
938 Laajoki, K., 2005. Karelian supracrustal rocks. In: Lehtinen, M., Nurmi, P., Rämö, T. (eds.) *The*
939 *Precambrian Bedrock of Finland – Key to the Evolution of the Fennoscandian Shield*.
940 Elsevier Science B.V., Amsterdam, pp. 279–342. https://doi.org/10.1016/S0166-
941 2635(05)80008-8
942 Lassiter, J. C., Byerly, B. L., Snow, J. E. & Hellebrand, E. (2014). Constraints from Os-isotope
943 variations on the origin of Lena Trough abyssal peridotites and implications for the
944 composition and evolution of the depleted upper mantle. *Earth and Planetary Science*
945 *Letters 403*, 178-187. https://doi.org/10.1016/j.epsl.2014.05.033
946 Li, Z. X. A. & Lee, C. T. A. (2006). Geochemical investigation of serpentinized oceanic
947 lithospheric mantle in the Feather River Ophiolite, California: implications for the recycling
948 rate of water by subduction. *Chemical Geology 235*(1-2), 161-185.
949 https://doi.org/10.1016/j.chemgeo.2006.06.011
950 Liu, C. Z., Snow, J. E., Hellebrand, E., Brügmann, G., Von Der Handt, A., Büchl, A. &
951 Hofmann, A. W. (2008). Ancient, highly heterogeneous mantle beneath Gakkel ridge, Arctic
952 Ocean. *Nature 452*(7185), 311-316. DOI:10.1038/nature06688

Liu, C.-Z., H. J. B., Mitchell, R. N., Wei, W., Zhang, Z.-Y., Hofmann, A. W., Yang, J.-F. & Li, Y. (2022). Archean cratonic mantle recycled at a mid-ocean ridge. *Science Advances 8*(22), eabn6749. DOI: 10.1126/sciadv.abn6749

Luguet, A., & Pearson, D. G. (2019). Dating mantle peridotites using Re-Os isotopes: The complex message from whole rocks, base metal sulfides, and platinum group minerals. *American Mineralogist 104*(2), 165-189. https://doi.org/10.2138/am-2019-6557

Malvoisin, B. (2015). Mass transfer in the oceanic lithosphere: serpentinization is not isochemical. *Earth and Planetary Science Letters 430*, 75-85. https://doi.org/10.1016/j.epsl.2015.07.043

McCoy-West, A. J., Bennett, V. C., Puchtel, I. S. & Walker, R. J. (2013). Extreme persistence of cratonic lithosphere in the southwest Pacific: Paleoproterozoic Os isotopic signatures in Zealandia. *Geology 41*(2), 231-234. https://doi.org/10.1130/G33626.1

Meisel, T., Walker, R. J., Irving, A. J. & Lorand, J. P. (2001). Osmium isotopic compositions of mantle xenoliths: a global perspective. *Geochimica et Cosmochimica Acta 65*(8), 1311-1323. https://doi.org/10.1016/S0016-7037(00)00566-4

Melcher, F. & Meisel, T. (2004). A metamorphosed early Cambrian crust–mantle transition in the Eastern Alps, Austria. *Journal of Petrology 45*(8), 1689-1723. https://doi.org/10.1093/petrology/egh030

Mertzman, S. A. (2000). K-Ar results from the southern Oregon-northern California Cascade Range. *Oregon Geology 62*(4), 99-122.

O'Driscoll, B., Day, J. M. D., Walker, R. J., Daly, J. S., McDonough, W. F. & Piccoli, P. M. (2012). Chemical heterogeneity in the upper mantle recorded by peridotites and chromitites from the Shetland Ophiolite Complex, Scotland. *Earth and Planetary Science Letters 333*, 226-237. https://doi.org/10.1016/j.epsl.2012.03.035

O'Driscoll, B., Walker, R. J., Day, J. M. D., Ash, R. D. & Daly, J. S. (2015). Generations of melt extraction, melt–rock interaction and high-temperature metasomatism preserved in peridotites of the ~497 Ma Leka Ophiolite Complex, Norway. *Journal of Petrology 56*(9), 1797-1828. https://doi.org/10.1093/petrology/egv055

O'Driscoll, B., Walker, R. J., Clay, P. L., Day, J. M. D., Ash, R. D. & Daly, J. S. (2018). Length-scales of chemical and isotopic heterogeneity in the mantle section of the Shetland Ophiolite Complex, Scotland. *Earth and Planetary Science Letters 488*, 144-154. https://doi.org/10.1016/j.epsl.2018.02.020

Paquet, M., Day, J. M., Brown, D. B., & Waters, C. L. (2022). Effective global mixing of the highly siderophile elements into Earth's mantle inferred from oceanic abyssal peridotites. *Geochimica et Cosmochimica Acta*, *316*, 347-362. https://doi.org/10.1016/j.gca.2021.09.033

Pearce, J. A. & Parkinson, I. J. (1993). Trace element models for mantle melting: application to volcanic arc petrogenesis. *Geological Society, London, Special Publications 76*(1), 373-403. https://doi.org/10.1144/GSL.SP.1993.076.01.19

Pearce, J. A. (2008). Geochemical fingerprinting of oceanic basalts with applications to ophiolite classification and the search for Archean oceanic crust. *Lithos 100*(1-4), 14-48. https://doi.org/10.1016/j.lithos.2007.06.016

Pearson, D. G., Canil, D. & Shirey, S. B. (2003). Mantle samples included in volcanic rocks: xenoliths and diamonds. *Treatise on Geochemistry 2*, 568. DOI: 10.1016/B0-08-043751-6/02005-3

998 Pearson, D. G., Irvine, G. J., Ionov, D. A., Boyd, F. R. & Dreibus, G. E. (2004). Re–Os isotope
999 systematics and platinum group element fractionation during mantle melt extraction: a study
1000 of massif and xenolith peridotite suites. *Chemical Geology 208*(1-4), 29-59.
1001 https://doi.org/10.1016/j.chemgeo.2004.04.005
1002 Pearson, D. G., Parman, S. W. & Nowell, G. M. (2007). A link between large mantle melting
1003 events and continent growth seen in osmium isotopes. *Nature 449*(7159), 202-205.
1004 DOI: 10.1038/nature06122
1005 Peltonen, P., Kontinen, A. & Huhma, H. (1996). Petrology and geochemistry of metabasalts
1006 from the 1.95 Ga Jormua ophiolite, northeastern Finland. *Journal of Petrology 37*(6), 1359-
1007 1383. https://doi.org/10.1093/petrology/37.6.1359
1008 Peltonen, P., Kontinen, A. & Huhma, H. (1998). Petrogenesis of the mantle sequence of the
1009 Jormua ophiolite (Finland): melt migration in the upper mantle during Palaeoproterozoic
1010 continental break-up. *Journal of Petrology 39*(2), 297-329.
1011 https://doi.org/10.1093/petroj/39.2.297
1012 Peltonen, P., Mänttäri, I., Huhma, H. & Kontinen, A. (2003). Archean zircons from the mantle:
1013 the Jormua ophiolite revisited. *Geology 31*(7), 645-648. https://doi.org/10.1130/0091-
1014 7613(2003)031<0645:AZFTMT>2.0.CO;2
1015 Peltonen, P. & Kontinen, A. (2004). The Jormua ophiolite: A mafic-ultramafic complex from an
1016 ancient ocean-continent transition zone. In: Kusky, T. M. (ed.) Precambrian Ophiolites and
1017 Related Rocks. *Developments in Precambrian Geology 13*, Elevier, Amsterdam, pp. 35-71.
1018 https://doi.org/10.1016/S0166-2635(04)13001-6
1019 Peltonen, P. (2005). Ophiolites. In: Lehtinen, M., Nurmi, P., Rämö, T. (eds.) *The Precambrian*
1020 *Bedrock of Finland – Key to the Evolution of the Fennoscandian Shield*. Elsevier Science
1021 B.V., Amsterdam, pp. 237-277.
1022 Rudnick, R. L. & Walker, R. J. (2009). Interpreting ages from Re–Os isotopes in peridotites.
1023 *Lithos 112*, 1083-1095. DOI:10.1016/j.lithos.2009.04.042
1024 Säntti, J., Kontinen, A., Sorjonen-Ward, P., Johanson, B. & Pakkanen, L. (2006). Metamorphism
1025 and chromite in serpentinized and carbonate-silica-altered peridotites of the Paleoproterozoic
1026 Outokumpu-Jormua ophiolite belt, eastern Finland. *International Geology Review 48*, 494-
1027 546. DOI:10.2747/0020-6814.48.6.494
1028 Schulte, R. F., Schilling, M., Anma, R., Farquhar, J., Horan, M. F., Komiya. T., Piccoli, P. M.,
1029 Pitcher, L. & Walker, R. J. (2009). Chemical and chronologic complexity in the convecting
1030 upper mantle: Evidence from the Taitao ophiolite, southern Chile. *Geochimica et*
1031 *Cosmochimica Acta* 73(19), 5793-5819. https://doi.org/10.1016/j.gca.2009.06.015
1032 Scott, D. J., Helmstaedt, H. & Bickle, M. J. (1992). Purtuniq ophiolite, Cape Smith belt, northern
1033 Quebec, Canada: A reconstructed section of Early Proterozoic oceanic crust. *Geology 20*(2),
1034 173-176. https://doi.org/10.1130/0091-7613(1992)020<0173:POCSBN>2.3.CO;2
1035 Secchiari, A., Gleissner, P., Li, C., Goncharov, A., Milke, R., Becker, H., Bosch, D. &
1036 Montanini, A., (2020). Highly siderophile and chalcophile element behaviour in abyssal-type
1037 and supra-subduction zone mantle: New insights from the New Caledonia
1038 ophiolite. *Lithos 354*, 105338. https://doi.org/10.1016/j.lithos.2019.105338
1039 Şengör, A. M. C. & Natal'in, B. A. (2004). Phanerozoic analogues of Archaean oceanic
1040 basement fragments: Altaid ophiolites and ophirags. *Developments in Precambrian*
1041 *Geology*, *13*, 675-726. https://doi.org/10.1016/S0166-2635(04)13021-1
1042 Shi, R., Alard, O., Zhi, X., O'Reilly, S. Y., Pearson, N. J., Griffin, W. L., Zhang, M. & Chen, X.
1043 (2007). Multiple events in the Neo-Tethyan oceanic upper mantle: Evidence from Ru–Os–Ir

alloys in the Luobusa and Dongqiao ophiolitic podiform chromitites, Tibet. *Earth and Planetary Science Letters 261*(1-2), 33-48. DOI: 10.1016/j.epsl.2007.05.044

Shields, G. & Stille, P. (2001). Diagenetic constraints on the use of cerium anomalies as palaeoseawater redox proxies: an isotopic and REE study of Cambrian phosphorites. *Chemical Geology 175*(1-2), 29-48. https://doi.org/10.1016/S0009-2541(00)00362-4

Shirey, S. B. & Walker, R. J. (1995). Carius tube digestion for low-blank rhenium-osmium analysis. *Analytical Chemistry 67*(13), 2136-2141. https://doi.org/10.1021/ac00109a036

Shirey, S. B. & Walker, R. J. (1998). The Re-Os isotope system in cosmochemistry and high-temperature geochemistry. *Annual Review of Earth and Planetary Sciences 26*(1), 423-500. DOI: 10.1146/annurev.earth.26.1.423

Snortum, E. & Day, J. M. D. (2020). Forearc origin for Coast Range Ophiolites inferred from osmium isotopes and highly siderophile elements. *Chemical Geology 550*, 119723. https://doi.org/10.1016/j.chemgeo.2020.119723

Snow, J. E. & Reisberg, L. (1995). Os isotopic systematics of the MORB mantle: results from altered abyssal peridotites. *Earth and Planetary Science Letters 133*(3-4), 411-421. https://doi.org/10.1016/0012-821X(95)00099-X

Snow, J. E., Schmidt, G. & Rampone, E. (2000). Os isotopes and highly siderophile elements (HSE) in the Ligurian ophiolites, Italy. *Earth and Planetary Science Letters 175*(1-2), 119-132. https://doi.org/10.1016/S0012-821X(99)00280-0

Stepanova, A. V., Samsonov, A. V., Salnikova, E. B., Puchtel, I. S., Larionova, Y. O., Larionov, A. N., Stepanov, V. S., Shapovalov, Y. B. & Egorova, S. V. (2014). Palaeoproterozoic continental MORB-type tholeiites in the Karelian Craton: petrology, geochronology, and tectonic setting. *Journal of Petrology 55*(9), 1719-1751. https://doi.org/10.1093/petrology/egu039

Stern, R. A., Syme, E. C. & Lucas, S. B. (1995). Geochemistry of 1.9 Ga MORB-and OIB-like basalts from the Amisk collage, Flin Flon belt, Canada: Evidence for an intra-oceanic origin. *Geochimica et Cosmochimica Acta 59*(15), 3131-3154. https://doi.org/10.1016/0016-7037(95)00202-B

Sun, S.-S. & McDonough, W. F. (1989). Chemical and isotopic systematics of oceanic basalts: implications for mantle composition and processes. *Geolological Society of London, Special Publications 42*, 313–345. doi:10.1144/GSL.SP.1989.042.01.19

Tsuru, A., Walker, R. J., Kontinen, A., Peltonen, P. & Hanski, E. (2000). Re-Os isotopic systematics of the 1.95 Ga Jormua ophiolite complex, northeastern Finland. *Chemical Geology 164*, 123–141. doi:10.1016/S0009-2541(99)00134-5

Uysal, İ., Ersoy, E. Y., Karslı, O., Dilek, Y., Sadıklar, M. B., Ottley, C. J., Tiepolo, M. & Meisel, T. (2012). Coexistence of abyssal and ultra-depleted SSZ type mantle peridotites in a Neo-Tethyan Ophiolite in SW Turkey: Constraints from mineral composition, whole-rock geochemistry (major–trace–REE–PGE), and Re–Os isotope systematics. *Lithos 132*, 50-69. https://doi.org/10.1016/j.lithos.2011.11.009

Vander Auwera, J. & André, L. (1991). Trace elements (REE) and isotopes (O, C, Sr) to characterize the metasomatic fluid sources: evidence from the skarn deposit (Fe, W, Cu) of Traversella (Ivrea, Italy). *Contributions to Mineralogy and Petrology 106*(3), 325-339.

Walker, R. J., Carlson, R. W., Shirey, S. B. & Boyd, F. R. (1989). Os, Sr, Nd, and Pb isotope systematics of southern African peridotite xenoliths: implications for the chemical evolution

of subcontinental mantle. *Geochimica et Cosmochimica Acta 53*(7), 1583-1595. https://doi.org/10.1016/0016-7037(89)90240-8

Walker, R. J., Hanski, E., Vuollo, J. & Liipo, J. (1996). The Os isotopic composition of Proterozoic upper mantle: evidence for chondritic upper mantle from the Outokumpu ophiolite, Finland. *Earth and Planetary Science Letters 141*(1-4), 161-173. https://doi.org/10.1016/0012-821X(96)00076-3

Walker, R. J., Prichard, H. M., Ishiwatari, A. & Pimentel, M. (2002). The osmium isotopic composition of convecting upper mantle deduced from ophiolite chromites. *Geochimica et Cosmochimica Acta 66*(2), 329-345. https://doi.org/10.1016/S0016-7037(01)00767-0

Walker, R. J. (2009). Highly siderophile elements in the Earth, Moon and Mars: update and implications for planetary accretion and differentiation. *Geochemistry 69*(2), 101-125. https://doi.org/10.1016/j.chemer.2008.10.001

Walker, R. J. (2016). Siderophile elements in tracing planetary formation and evolution. *Geochemical Perspectives 5*(1), 1. doi: 10.7185/geochempersp.5.1

Xiong, Y., Wood, S. & Kruszewski, J. (2006). Hydrothermal transport and deposition of rhenium under subcritical conditions revisited. *Economic Geology 101*(2), 471-478. https://doi.org/10.2113/gsecongeo.101.2.471

Xu, Y., Liu, J., Xiong, Q., Su, B. X., Scott, J. M., Xu, B., Zhu, D. C. & Pearson, D. G. (2020). The complex life cycle of oceanic lithosphere: A study of Yarlung-Zangbo ophiolitic peridotites, Tibet. *Geochimica et Cosmochimica Acta 277*, pp.175-191. https://doi.org/10.1016/j.gca.2020.03.024

Zhai, M., Zhao, G. & Zhang, Q. (2002). Is the Dongwanzi complex an Archean ophiolite? *Science 295*(5557), 923-923. DOI: 10.1126/science.1059426

Zhang, H. F., Goldstein, S. L., Zhou, X. H., Sun, M., Zheng, J. P. & Cai, Y. (2008). Evolution of subcontinental lithospheric mantle beneath eastern China: Re–Os isotopic evidence from mantle xenoliths in Paleozoic kimberlites and Mesozoic basalts. *Contributions to Mineralogy and Petrology 155*, 271-293.

Zhao, G., Wilde, S. A., Li, S., Sun, M., Grant, M. L. & Li, X. (2007). U–Pb zircon age constraints on the Dongwanzi ultramafic–mafic body, North China, confirm it is not an Archean ophiolite. *Earth and Planetary Science Letters 255*(1-2), 85-93. https://doi.org/10.1016/j.epsl.2006.12.007

FIGURE CAPTIONS

Figure 1. Location of the Jormua Ophiolite complex in the Kainuu belt. The dashed line shows the inferred position of the S-W margin of the Archean Karelia craton. The Jomua Ophiolite Complex is labeled on the map as "JOC", and the Outokumpu Ophiolite Complex is labeled as "OOC."

Figure 2. Geological map of the Jormua area (modified after Kontinen, 1998) with sample locations. HaB = Hannusranta block, LeB = Lehmivaara block, KaB = Kannas block, AnB = Antinmäki block.

Figure 3. Field photos showing the grid sample outcrops and sample sites. Locations of each grid are shown in **Figure 2**. Note the presence of ultramafic veins in the Grid 2 outcrop.

Figure 4. Major element (anhydrous) variations in the JOC harzburgites. Background data for oceanic lithosphere (closed green circles) and cratonic lithosphere (open black circles) are from a compilation provided bv Jingao Liu (see **Electronic Supplement** for data sources). **A**. Al_2O_3 vs. MgO. **B**. TiO_2 vs. MgO. Most of the Grid 1 TiO_2 contents are below detection limits and are not plotted. **C**. P_2O_5 vs. MgO. Grids 1 and most of 2 have P_2O_5 below detection limits and are not plotted. **D**. LOI vs. MgO. High LOI in Grid 3 and some of the non-grid harzburgites is comparable to higher LOI at higher MgO in the background dataset (see inset). Grid 3 is also notable because of its high average MgO, CaO, P_2O_5, and Al_2O_3, and low SiO_2 compared to other JOC harzburgites. **E.** MgO/SiO_2 vs. Al_2O_3/SiO_2.

Figure 5. Primitive mantle-normalized trace element patterns, sorted by grid. Individual samples within each grid are plotted as thin purple lines, and grid median is shown as thicker black lines. **A**. Grid 1 (Antinmäki). **B**. Grid 2 (Antinmäki). **C**. Grid 3 (Antinmäki). **D**. Grid 4 (Lehmivaara). **E**. Non-grid harzburgites.

Figure 6. PM-normalized rare earth element patterns, sorted by grid. Individual samples are shown as thin purple lines, and grid medians are given as thicker black lines. Median REE patterns of background oceanic lithosphere and cratonic lithosphere are also shown (from compilation provided by Jingao Liu). Thin black lines are representative E-DMM (enriched Depleted MORB Mantle), DMM (Depleted MORB Mantle), and D-DMM (depleted MORB Mantle) plotted for comparison, after Workman & Hart (2005). **A**. Grid 1 (Antinmäki). **B**. Grid 2 (Antinmäki). **C**. Grid 3 (Antinmäki). **D**. Grid 4 (Lehmivaara). **E**. Non-grid harzburgite samples.

Figure 7. Niobium/U vs. Nb/Yb. Arrows indicate expected vectors for U-mobility compared to source enrichment.

Figure 8. PM-normalized HSE concentrations, sorted by grid. Median and 2SE (median) are also shown for all JOC harzburgites to compare extent of heterogeneity within a grid to that characterized for the entire ophiolite (proxying kilometer scale variability). **A**. Grid 1 (Antinmäki). **B**. Grid 2 (Antinmäki). **C**. Grid 3 (Antinmäki). **D**. Grid 4 (Lehmivaara). **E**. Non-grid harzburgite samples. The 2SE of the median is calculated as $1.253*(2\sigma_{mean}/\mathrm{sqrt}(N))$, where σ_{mean} is the standard deviation of the mean, and N is the number of samples in the population.

Figure 9. A. PM-normalized Re/Pd vs. Re, showing a correlation between increasing Re abundance and superchondritic Re/Pd, indicative of secondary Re re-enrichment. In some cases, notably with Grid 2, this re-enrichment correlates with poor agreement between T_{MA}, T_{RD1}, and T_{RD2}. Most of the rest of the samples lack evidence of Re modification and all three model ages tend to fall within ~0.3 Gyr (see **Table 1**). **B.** PM-normalized Re/Ir vs. Pd/Ir, showing that, with the exception of most of Grid 2 and several other outlying samples, JOC harzburgites are typically depleted in both elements compared to PM. This also confirms that elevated Re/Pd in panel. **A** is controlled by elevated Re, and Pd is not unusually depleted in any high Re/Pd samples. Further, no systematic variation between Re and Pd is apparent.

Figure 10. A. $^{187}Re/^{188}Os$ vs. γOs_t of JOC harzburgites. Elevated $^{187}Re/^{188}Os$ (> ~0.2 in JOC harzburgites) in some samples implies that the ^{187}Re-^{187}Os system was disrupted at some point after the lithospheric mantle was generated, but trajectories (black arrows) suggest that samples in different locations within the ophiolite may have been affected differently. Most of the Grid 2 samples, a Grid 4 sample, and one of the non-grid harzburgite samples (JU15-1) have elevated $^{187}Re/^{188}Os$. The latter two samples have excess Re and so overcorrected initial $^{187}Os/^{188}Os$ relative to the rest of the harzburgites, whereas Grid 2 $^{187}Os/^{188}Os$ are indistinguishable from rest of the data. **B.** T_{RD2} vs. T_{MA}, illustrating which samples have good agreement between the two model approaches. Samples plotting the furtherst from the 1:1 correlation line are the same samples shown to have Re re-addition in **Figure 9**. One non-grid sample (ATK96) gave a T_{MA} of 63 Ga and JU15-18 B3 from Grid 2 gave a T_{MA} of 5.1 Ga, both of which are erroneously old and not shown. **C.** Similar to panel **B**, except comparing T_{RD1} vs. T_{RD2}. In T_{RD1}, a majority of the Grid 2 samples give negative (future) model ages and are not shown on this plot. Stacked

histograms for γOs_t and all three age methods are shown with plots to show median and distribution of the samples by grid (and the non-grid harzburgite group).

Figure 11. Thorium/Yb vs. Nb/Yb after Pearce et al. (2008). Covarying Th-Nb enrichments (relative to Yb) proxy source enrichment. The JOC samples a heterogeneous, enriched mantle source relative to MORB-type compositions. Grids 3 and 4 plot near E-MORB, while Grid 2 plots between N-MORB and E-MORB. Grid 1 Th is below detection limits and not plotted.

Figure 12. A) Titanium vs. Yb and **B**) V vs. Yb, demonstrating depth of melting and oxidation state and mantle fertility for JOC harzburgites. Melting models and compositions are from Pearce and Parkinson (1993). FMM = Fertile MORB Mantle. RMM = Refractory MORB Mantle. EFM = Enriched Fertile Mantle. ERM = Enriched Refractory mantle. Quartz-Fayalite-Magnetite (QFM; thin black lines) models are shown for FMM. Depletion trajectories for enriched and fertile mantle (grey stippled lines) are also shown. While V vs. Yb (**B**) records variable oxygen fugacity and/or mantle enrichment, it does not easily distinguish the two. Titanium vs. Yb (**A**) may distinguish enriched and depleted mantle as well as depth of melting. See **Discussion** for details.

Figure 13. A. Pt_N/Os_N vs. Eu/Eu*. **B**. Ir_N/Os_N vs. Eu/Eu*. In this space, negative anomalies (<1) in both indices are often diagnostic of Type 2 harzburgite. **C**. γOs_t vs. Eu/Eu*. Although a weaker correlation than seen in **B**, γOs_t and Eu/Eu* differ between Type 1 and Type 2 harzburgites. The Type 1 outliers are likelier to skew to higher γOs_t while Type 2 outliers are likelier to skew to lower γOs_t.

Figure 14. γOs_t vs. obduction age of a global ophiolite compilation. Harzburgites (dark blue circles) and chromites (light grey circles) are shown; see **Table 3** for details. Each ophiolite is shown as a median γOs_t, with error bars representing the standard error of the median. Models of the evolution of the abyssal mantle reservoir (dashed grey line after Haller et al., 2021) and PM (solid grey line: after Meisel et al., 2001) are shown for reference. The JOC Type 1 γOs_t value plots within the compositional range of modern ophiolites and depleted by roughly 2% relative to the chondritic reference ($\gamma Os_t = 0$). Data sources for compilation: Snow et al., 2000; Büchl et al., 2002; Walker et al., 2002; Melcher and Meisel, 2004; Frei et al., 2006; Agranier et al., 2007; Kusky et al., 2007; Shi et al., 2007; Schulte et al., 2009; Uysal et al., 2012; O'Driscoll et al., 2012, 2015, 2018; Gonzáles-Jiménez et al., 2014; Gong et al., 2020; Secchiari et al., 2020; Snortum and Day, 2020; Xu et al., 2020; Haller et al., 2021.

Table 1. Highly siderophile element data (ppb) and Re-Os systematics for JOC serpentinized harzburgites.

Sample	Block	Type	Os	Ir	Ru	Pt	Pd	Re		Os/Ir	Ru/Ir	Pt/Ir	Pd/Ir	Os_N/Ir_N	Ru_N/Ir_N	Pt_N/Ir_N	Pd_N/Ir_N	Re_N/Ir_N	Re_N/Pd_N	Ir/Ir*	Pt/Pt*	$^{187}Os/^{188}Os$	±2SE	%2SE	$^{187}Os/^{188}Os_i$	$^{187}Re/^{188}Os$	$\gamma Os_{1.95\,Ga}$	T_{MA} (Ga)	T_{RD1} (Ga)	T_{RD2} (Ga)
Non-grid harzburgites																														
JU15-23†	Antinmäki	1, LREE-enrich		4.130	6.432	13.28	3.940	9.870	0.067		0.6	2.1	0.6	1.5	0.6	0.9	0.3	1.0	0.1	0.1	1.3	0.3	0.1184	7.8E-05	0.07	0.1158	0.078	1.8	1.6	1.3	1.7
ATK57-A*	Antinmäki	1, LREE-enrich		3.254	4.456	5.689	7.718	3.844	0.034		0.7	1.3	1.7	0.9	0.7	0.6	0.8	0.6	0.1	0.2	1.6	1.4	0.1159	-	*0.20*	0.1142	0.050	0.5	1.9	1.6	1.9
ATK57-B*	Antinmäki	1, LREE-enrich		4.037	3.544	7.517	4.738	3.015	0.037		1.1	2.1	1.3	0.9	1.1	1.0	0.6	0.6	0.1	0.2	1.0	0.9	0.1157	-	*0.20*	0.1143	0.044	0.5	1.9	1.7	1.9
ATK59*	Antinmäki	2		2.665	2.386	5.065	3.877	2.341	0.112		1.1	2.1	1.6	1.0	1.0	1.0	0.8	0.7	0.6	0.8	1.0	1.0	0.1174	-	*0.20*	0.1107	0.203	-2.7	2.9	1.4	2.4
ATK75*	Antinmäki	1, LREE-enrich		4.820	3.877	9.206	4.456	1.842	0.033		1.2	2.4	1.1	0.5	1.1	1.1	0.6	0.3	0.1	0.3	0.9	0.9	0.1115	-	*0.20*	0.1104	0.033	-2.9	2.5	2.3	2.4
ATK76*	Antinmäki	1, LREE-deplet		6.159	4.422	1.656	4.976	1.120	0.052		1.4	0.4	1.1	0.3	1.3	0.2	0.5	0.2	0.1	0.8	2.1	3.2	0.1113	-	*0.20*	0.1100	0.040	-3.3	2.6	2.3	2.5
ATK96*	Antinmäki	1, LREE-deplet		3.457	3.020	7.451	6.037	3.105	0.284		1.1	2.5	2.0	1.0	1.1	1.1	1.0	0.7	1.1	1.6	0.9	1.1	0.1146	-	*0.20*	0.1016	0.395	-11	63	1.8	3.7
ATK589*	Antinmäki	2		10.84	5.605	9.336	6.715	2.575	0.030		1.9	1.7	1.2	0.5	1.8	0.8	0.6	0.3	0.1	0.2	0.9	1.2	0.1111	-	*0.20*	0.1107	0.014	-2.7	2.4	2.3	2.4
ATK600*	Antinmäki	1, LREE-enrich		3.623	1.815	4.052	3.587	2.071	0.046		2.0	2.2	2.0	1.1	1.8	1.0	0.9	0.8	0.3	0.4	0.7	1.1	0.1176	-	*0.20*	0.1156	0.061	1.6	1.7	1.4	1.7
JU15-1†	Hannusranta	2		3.041	3.885	5.520	5.52	1.494	0.400		0.8	1.4	1.4	0.4	0.7	0.6	0.7	0.3	1.2	4.7	1.5	1.7	0.1317	9.7E-05	0.07	0.1107	0.634	-2.7	1.2	-0.7	2.4
JU15-1dup†	Hannusranta	2		1.899	-	-	-	-	0.611		-	-	-	-	-	-	-	-	-				0.1467	1.1E-04	0.07	0.0952	1.554	-16	1.0	-3.0	4.6
mean non-grid				**4.546**	**3.944**	**6.877**	**5.156**	**3.128**	**0.120**		**1.2**	**1.8**	**1.4**	**0.8**	**1.1**	**0.8**	**0.7**	**0.5**	**0.4**	**0.9**	**1.2**	**1.3**	**0.1173**			**0.1106**	**0.201**	**-2.7**	**8.2**	**1.4**	**2.4**
2SD				**4.912**	**2.783**	**6.498**	**2.681**	**5.006**	**0.312**		**0.9**	**1.3**	**0.9**	**0.8**	**0.9**	**0.6**	**0.4**	**0.5**	**0.9**	**2.8**	**0.9**	**1.5**	**0.0163**			**0.0099**	**0.669**	**8.7**	**38.6**	**2.4**	**1.4**
median non-grid				**3.830**	**3.881**	**6.570**	**4.857**	**2.458**	**0.049**		**1.1**	**2.1**	**1.4**	**0.9**	**1.1**	**1.0**	**0.7**	**0.6**	**0.1**	**0.4**	**1.0**	**1.1**	**0.1158**			**0.1107**	**0.056**	**-2.7**	**2.2**	**1.6**	**2.4**
1SE(median)				**0.973**	**0.551**	**1.287**	**0.531**	**0.992**	**0.062**		**0.2**	**0.3**	**0.2**	**0.2**	**0.2**	**0.1**	**0.1**	**0.1**	**0.2**	**0.6**	**0.2**	**0.3**	**0.0032**			**0.0020**	**0.133**	**1.7**	**7.7**	**0.5**	**0.3**
median non-grid Type 1																										**0.1142**	**0.050**	**0.5**	**1.9**	**1.7**	**1.9**
1SE(median)																										**0.0024**	**0.062**	**2.1**	**10.9**	**0.2**	**0.3**
median non-grid Type 2																										**0.1107**	**0.203**	**-2.7**	**2.4**	**1.4**	**2.4**
1SE(median)																										**0.0032**	**0.417**	**2.8**	**0.7**	**1.6**	**0.5**
Grid 1																															
JU15-16 A1‡	Antinmäki			1.838	7.222	9.525	6.543	6.799	0.007		0.3	1.3	0.9	0.9	0.2	0.6	0.4	0.6	0.0	0.0	2.7	0.7	0.1119	-	*0.20*	0.1113	0.018	-2.1	2.3	2.2	2.4
JU15-16 A2‡	Antinmäki			3.358	5.984	40.34	6.200	6.642	0.009		0.6	6.7	1.0	1.1	0.5	3.1	0.5	0.8	0.0	0.0	0.8	0.3	0.1117	-	*0.20*	0.1112	0.012	-2.2	2.3	2.3	2.4
JU15-16 A2dup‡	Antinmäki			4.943	6.111	38.93	6.479	6.574	0.017		0.8	6.4	1.1	1.1	0.7	2.9	0.5	0.7	0.0	0.0	0.7	0.3	0.1112	-	*0.20*	0.1106	0.017	-2.7	2.4	2.3	2.5
JU15-16 A3‡	Antinmäki			1.860	3.778	4.371	13.860	6.620	0.005		0.5	1.2	3.7	1.8	0.5	0.5	1.8	1.2	0.0	0.0	2.0	2.2	0.1132	-	*0.20*	0.1128	0.012	-0.8	2.1	2.0	2.2
JU15-16 B1‡	Antinmäki			1.787	4.072	10.14	9.673	3.512	0.019		0.4	2.5	2.4	0.9	0.4	1.1	1.1	0.6	0.1	0.1	1.5	1.4	0.1120	-	*0.20*	0.1104	0.050	-3.0	2.5	2.2	2.5
JU15-16 B2‡	Antinmäki			2.076	4.117	10.29	9.723	3.561	0.019		0.5	2.5	2.4	0.9	0.5	1.1	1.1	0.6	0.1	0.1	1.4	1.4	0.1120	-	*0.20*	0.1105	0.045	-2.8	2.5	2.2	2.5
JU15-16 B3‡	Antinmäki			2.534	3.079	7.724	7.427	1.094	0.016		0.8	2.5	2.4	0.4	0.8	1.1	1.2	0.2	0.1	0.3	1.1	2.2	0.1119	-	*0.20*	0.1109	0.031	-2.5	2.4	2.2	2.4
JU15-16 C1‡	Antinmäki			9.004	4.063	5.464	3.357	0.446	0.031		2.2	1.3	0.8	0.1	2.0	0.6	0.4	0.1	0.1	1.2	0.9	1.9	0.1120	-	*0.20*	0.1114	0.016	-2.0	2.3	2.2	2.4
JU15-16 C2‡	Antinmäki			5.270	1.193	5.637	2.950	1.123	0.027		4.4	4.7	2.5	0.9	4.1	2.2	1.2	0.6	0.3	0.4	0.3	1.0	0.1138	-	*0.20*	0.1130	0.024	-0.7	2.1	1.9	2.1
JU15-16 C3‡	Antinmäki			1.590	7.472	5.537	2.749	0.242	0.017		0.2	0.7	0.4	0.0	0.2	0.3	0.2	0.0	0.0	1.2	3.9	2.0	0.1132	-	*0.20*	0.1115	0.052	-2.0	2.3	2.0	2.4
mean Grid 1				**3.346**	**4.560**	**10.92**	**6.958**	**3.334**	**0.017**		**1.1**	**2.6**	**1.8**	**0.8**	**1.0**	**1.2**	**0.9**	**0.5**	**0.1**	**0.4**	**1.6**	**1.5**	**0.1124**			**0.1114**	**0.029**	**-2.0**	**2.3**	**2.1**	**2.4**
2SD				**4.931**	**4.037**	**21.99**	**7.422**	**5.541**	**0.017**		**2.8**	**3.8**	**2.2**	**1.1**	**2.5**	**1.7**	**1.0**	**0.7**	**0.2**	**1.0**	**2.2**	**1.4**	**0.0016**			**0.0019**	**0.032**	**1.6**	**0.3**	**0.2**	**0.3**
median Grid 1				**2.076**	**4.072**	**7.72**	**6.543**	**3.512**	**0.017**		**0.5**	**2.5**	**2.4**	**0.9**	**0.5**	**1.1**	**1.1**	**0.6**	**0.1**	**0.1**	**1.4**	**1.4**	**0.1120**			**0.1113**	**0.024**	**-2.1**	**2.3**	**2.2**	**2.4**
1SE(median)				**1.030**	**0.843**	**4.593**	**1.550**	**1.157**	**0.004**		**0.6**	**0.8**	**0.5**	**0.2**	**0.5**	**0.4**	**0.2**	**0.2**	**0.0**	**0.2**	**0.5**	**0.3**	**0.0003**			**0.0004**	**0.007**	**0.3**	**0.1**	**0.0**	**0.1**
Grid 2																															
JU15-18 A1‡	Antinmäki			1.677	2.051	5.957	3.135	1.928	0.220		0.8	2.9	1.5	0.9	0.8	1.3	0.7	0.6	1.3	2.0	1.0	0.8	0.1320	-	*0.20*	0.1112	0.632	-2.3	1.3	-0.8	2.4
JU15-18 A2‡	Antinmäki			1.555	2.651	5.146	3.155	0.952	0.190		0.6	1.9	1.2	0.4	0.5	0.9	0.6	0.2	0.9	3.5	1.4	1.2	0.1349	-	*0.20*	0.1155	0.589	1.5	2.5	-1.2	1.8
JU15-18 A3‡	Antinmäki			1.373	2.057	5.312	5.168	3.007	0.210		0.7	2.6	2.5	1.5	0.6	1.2	1.2	1.0	1.2	1.2	1.2	1.1	0.1380	-	*0.20*	0.1136	0.739	-0.1	1.9	-1.7	2.1
JU15-18 B1‡	Antinmäki			2.087	2.494	7.492	2.606	2.639	0.212		0.8	3.0	1.0	1.1	0.8	1.4	0.5	0.7	1.0	1.4	1.0	0.5	0.1287	-	*0.20*	0.1126	0.489	-1.0	1.1	-0.3	2.2
JU15-18 B2‡	Antinmäki			3.912	4.344	9.534	7.852	5.673	0.062		0.9	2.2	1.8	1.3	0.8	1.0	0.9	0.9	0.2	0.2	1.1	0.9	0.1256	-	*0.20*	0.1231	0.076	8.3	0.3	0.2	0.7
JU15-18 B3‡	Antinmäki			1.762	2.011	4.760	2.779	3.680	0.180		0.9	2.4	1.4	1.8	0.8	1.1	0.7	1.2	1.1	0.9	1.1	0.6	0.1352	-	*0.20*	0.1189	0.493	4.5	5.1	-1.2	1.3
JU15-18 C1‡	Antinmäki			3.337	3.202	6.165	5.521	1.142	0.247		1.0	1.9	1.7	0.4	1.0	0.9	0.8	0.2	0.9	3.8	1.1	1.8	0.1253	-	*0.20*	0.1135	0.356	-0.2	2.4	0.3	2.1
JU15-18 C2‡	Antinmäki			4.241	2.769	2.927	0.688	0.738	0.238		1.5	1.1	0.2	0.3	1.4	0.5	0.1	0.2	1.0	5.7	1.2	0.4	0.1189	-	*0.20*	0.1100	0.270	-3.3	3.6	1.2	2.6
JU15-18 C3‡	Antinmäki			1.928	2.893	5.881	7.214	2.734	0.310		0.7	2.0	2.5	0.9	0.6	0.9	1.2	0.6	1.3	2.0	1.3	1.6	0.1364	-	*0.20*	0.1108	0.776	-2.6	1.5	-1.4	2.5
mean Grid 2				**2.430**	**2.719**	**5.908**	**4.235**	**2.499**	**0.208**		**0.9**	**2.2**	**1.5**	**0.9**	**0.8**	**1.0**	**0.7**	**0.6**	**1.0**	**2.3**	**1.2**	**1.0**	**0.1306**			**0.1144**	**0.491**	**0.5**	**2.2**	**-0.5**	**2.0**
2SD				**2.187**	**1.474**	**3.665**	**4.702**	**3.120**	**0.133**		**0.6**	**1.2**	**1.4**	**1.1**	**0.5**	**0.5**	**0.7**	**0.7**	**0.7**	**3.5**	**0.3**	**1.0**	**0.0127**			**0.0085**	**0.453**	**7.5**	**2.9**	**1.9**	**1.2**
median Grid 2				**1.928**	**2.651**	**5.881**	**3.155**	**2.639**	**0.212**		**0.8**	**2.2**	**1.5**	**0.9**	**0.8**	**1.0**	**0.7**	**0.6**	**1.0**	**2.0**	**1.1**	**0.9**	**0.1320**			**0.1135**	**0.493**	**-0.2**	**1.9**	**-0.8**	**2.1**
1SE(median)				**0.457**	**0.308**	**0.765**	**0.982**	**0.651**	**0.028**		**0.1**	**0.2**	**0.3**	**0.2**	**0.1**	**0.1**	**0.1**	**0.2**	**0.1**	**0.7**	**0.1**	**0.2**	**0.0027**			**0.0018**	**0.095**	**1.6**	**0.6**	**0.4**	**0.3**
median Type 1 LREE-depleted																										**0.1109**	**0.031**	**-2.5**	**2.4**	**2.2**	**2.4**
1SE(median)																										**0.0012**	**0.042**	**1.0**	**6.9**	**0.1**	**0.2**
median Type 1 LREE-enriched																										**0.1136**	**0.313**	**-0.2**	**1.9**	**0.7**	**2.1**
1SE(median)																										**0.0015**	**0.085**	**1.3**	**4.8**	**0.4**	**0.2**
median Type 1 (all)																										**0.1115**	**0.052**	**-2.0**	**2.3**	**1.7**	**2.4**
1SE(median)																										**0.0010**	**0.065**	**0.8**	**3.1**	**0.3**	**0.1**
Grid 3																															
JU15-21 A1†	Antinmäki			2.838	1.377	7.600	1.340	1.500	0.016		2.1	5.5	1.0	1.1	1.9	2.5	0.5	0.7	0.1	0.2	0.5	0.3	0.1090	1.0E-04	0.09	0.1081	0.027	-4.9	2.8	2.6	2.8
JU15-21 A2†	Antinmäki			4.150	2.408	6.297	2.450	2.483	0.023		1.7	2.6	1.0	1.0	1.6	1.2	0.5	0.7	0.1	0.2	0.7	0.5	0.1097	8.1E-05	0.07	0.1088	0.026	-4.3	2.7	2.5	2.7
JU15-21 A3†	Antinmäki			5.008	2.524	10.875	7.280	5.292	0.034		2.0	4.3	2.9	2.1	1.8	2.0	1.4	1.4	0.2	0.1	0.5	0.8	0.1118	6.9E-05	0.06	0.1107	0.032	-2.7	2.4	2.2	2.4
JU15-21 B1†	Antinmäki			4.707	3.226	8.194	2.830	1.695	0.021		1.5	2.5	0.9	0.5	1.3	1.2	0.4	0.4	0.1	0.2	0.8	0.7	0.1086	5.7E-05	0.05	0.1079	0.021	-5.1	2.8	2.7	2.8
JU15-21 B2†	Antinmäki			2.810	2.613	6.354	5.850	3.445	0.034		1.1	2.4	2.2	1.3	1.0	1.1	1.1	0.9	0.2	0.2	1.0	1.1	0.1111	8.3E-05	0.07	0.1092	0.058	-4.0	2.7	2.3	2.6
JU15-21 B3†	Antinmäki			4.740	3.022	7.535	3.570	3.278	0.121		1.6	2.5	1.2	1.1	1.4	1.1	0.6	0.7	0.5	0.6	0.8	0.6	0.1106	7.0E-05	0.06	0.1066	0.122	-6.3	3.4	2.4	3.0
JU15-21 C1†	Antinmäki			3.879	3.552	8.343	2.590	1.849	0.027		1.1	2.3	0.7	0.5	1.0	1.1	0.4	0.4	0.1	0.3	1.0	0.6	0.1101	6.5E-05	0.06	0.1090	0.033	-4.1	2.7	2.5	2.6
JU15-21 C2†	Antinmäki			3.626	2.806	6.387	2.990	2.738	0.021		1.3	2.3	1.1	1.0	1.2	1.0	0.5	0.7	0.1	0.1	0.9	0.6	0.1101	7.3E-05	0.07	0.1091	0.028	-4.1	2.6	2.5	2.6
JU15-21 C3†	Antinmäki			3.971	1.846	7.402	2.180	2.359	0.008		2.2	4.0	1.2	1.3	2.0	1.8	0.6	0.9	0.1	0.1	0.5	0.5	0.1095	6.8E-05	0.06	0.1091	0.010	-4.1	2.6	2.6	2.6
JU15-21 C3dup†	Antinmäki			4.098	-	-	-	-	0.008		-	-	-	-	-	-	-	-	-	-	-	-	0.1093	7.7E-05	0.07	0.1090	0.009	-4.2	2.6	2.6	2.6
mean Grid 3				**3.977**	**2.597**	**7.665**	**3.453**	**2.738**	**0.034**		**1.6**	**3.2**	**1.3**	**1.1**	**1.5**	**1.4**	**0.6**	**0.7**	**0.2**	**0.2**	**0.7**	**0.6**	**0.1101**			**0.1087**	**0.040**	**-4.4**	**2.7**	**2.5**	**2.7**
2SD				**1.582**	**1.346**	**2.860**	**3.798**	**2.338**	**0.067**		**0.8**	**2.3**	**1.4**	**0.9**	**0.8**	**1.1**	**0.7**	**0.6**	**0.3**	**0.3**	**0.4**	**0.4**	**0.0020**			**0.0022**	**0.067**	**2.0**	**0.5**	**0.3**	**0.3**
median Grid 3				**4.035**	**2.613**	**7.535**	**2.830**	**2.483**	**0.023**		**1.6**	**2.5**	**1.1**	**1.1**	**1.4**	**1.2**	**0.5**	**0.7**	**0.1**	**0.2**	**0.8**	**0.6**	**0.1101**			**0.1090**	**0.028**	**-4.1**	**2.7**	**2.5**	**2.6**
1SE(median)				**0.330**	**0.281**	**0.597**	**0.793**	**0.488**	**0.014**		**0.2**	**0.5**	**0.3**	**0.2**	**0.2**	**0.2**	**0.1**	**0.1**	**0.1**	**0.1**	**0.1**	**0.1**	**0.0004**			**0.0005**	**0.014**	**0.4**	**0.1**	**0.1**	**0.1**
Grid 4																															
JU15-25†	Lehmivaara			4.440	4.600	10.210	3.011	2.170	0.045		1.0	2.2	0.7	0.5	0.9	1.0	0.3	0.3	0.1	0.4	1.1	0.6	0.1125	7.5E-05	0.07	0.1109	0.049	-2.5	2.4	2.1	2.4
JU15-25dup†	Lehmivaara			4.405	4.279	9.028	2.950	2.260	0.048		1.0	2.1	0.7	0.5	1.0	1.0	0.3	0.4	0.1	0.4	1.0	0.6	0.1125	9.1E-05	0.08	0.1107	0.052	-2.6	2.5	2.1	2.4
JU15-26†	Lehmivaara			5.530	4.230	8.330	2.636	1.999	0.045		1.3	2.0	0.6	0.5	1.2	0.9	0.3	0.3	0.1	0.4	1.0	0.6	0.1137	7.7E-05	0.07	0.1125	0.039	-1.1	2.2	1.9	2.1
JU15-27†	Lehmivaara			4.054	3.921	7.222	2.303	1.486	0.333		1.0	1.8	0.6	0.4	1.0	0.8	0.3	0.3	1.0	4.0	1.1	0.6	0.1153	1.2E-04	0.11	0.1022	0.396	-10		1.7	
JU15-28†	Lehmivaara			4.243	4.241	8.288	3.218	1.771	0.035		1.0	2.0	0.8	0.4	0.9	0.9	0.4	0.3	0.1	0.3	1.1	0.7	0.1122	8.2E-05	0.07	0.1109	0.040	-2.5	2.4	2.2	2.4
JU15-29†	Lehmivaara			4.484	4.277	8.489	7.441	6.066	0.051		1.0	2.0	1.7	1.4	1.0	0.9	0.8	1.0	0.1	0.1	1.1	0.9	0.1166	8.3E-05	0.07	0.1148	0.055	0.9	1.8	1.5	1.8
JU15-30†	Lehmivaara			4.311	3.016	7.495	2.920	2.315	0.229		1.4	2.5	1.0	0.8	1.3	1.1	0.5	0.5	0.9	1.7	0.8	0.6	0.1170	7.6E-05	0.06	0.1085	0.256	-4.6	3.9	1.5	2.7
mean Grid 4				**4.507**	**4.021**	**8.241**	**3.583**	**2.642**	**0.123**		**1.1**	**2.1**	**0.9**	**0.7**	**1.0**	**0.9**	**0.4**	**0.4**	**0.4**	**1.2**	**1.0**	**0.7**	**0.1146**			**0.1100**	**0.139**	**-3.3**	**2.5**	**1.8**	**2.3**
2SD				**1.046**	**1.040**	**1.689**	**3.832**	**3.408**	**0.254**		**0.4**	**0.5**	**0.9**	**0.8**	**0.3**	**0.2**	**0.4**	**0.5**	**0.9**	**3.0**	**0.2**	**0.3**	**0.0041**			**0.0086**	**0.302**	**7.6**	**1.6**	**0.6**	**0.7**

median Grid 4	**4.367**	**4.236**	**8.309**	**2.950**	**2.107**	**0.049**	**1.0**	**2.0**	**0.7**	**0.5**	**1.0**	**0.9**	**0.3**	**0.3**	**0.1**	**0.4**	**1.1**	**0.6**	**0.1145**	**0.1109**	**0.053**	**-2.5**	**2.4**	**1.8**	**2.4**
1SE(median)	**0.268**	**0.266**	**0.432**	**0.980**	**0.872**	**0.065**	**0.1**	**0.1**	**0.2**	**0.2**	**0.1**	**0.1**	**0.1**	**0.1**	**0.2**	**0.8**	**0.1**	**0.1**	**0.0011**	**0.0022**	**0.077**	**1.9**	**0.5**	**0.2**	**0.2**
median Type 2 (all)																				**0.1091**	**0.039**	**-4.1**	**2.6**	**2.3**	**2.6**
1SE(median)																				**0.0009**	**0.077**	**0.8**	**0.2**	**0.3**	**0.1**
mean harzburgite	**3.727**	**3.545**	**7.877**	**4.765**	**2.890**	**0.099**	**1.193**	**2.382**	**1.443**	**0.868**	**1.102**	**1.085**	**0.693**	**0.590**	**0.399**	**0.989**	**1.152**	**1.031**	**0.117**	**0.1111**	**0.183**	**-2.3**	**3.8**	**1.4**	**2.3**
2SD	**3.732**	**2.859**	**10.862**	**5.246**	**3.988**	**0.230**	**1.437**	**2.320**	**1.494**	**0.955**	**1.326**	**1.057**	**0.717**	**0.648**	**0.899**	**2.756**	**1.216**	**1.218**	**0.018**	**0.0077**	**0.517**	**6.8**	**19**	**2.6**	**1.0**
median harzburgite	**3.879**	**3.226**	**7.451**	**3.877**	**2.359**	**0.037**	**1.048**	**2.233**	**1.190**	**0.940**	**0.968**	**1.017**	**0.571**	**0.639**	**0.140**	**0.349**	**1.001**	**0.895**	**0.113**	**0.1108**	**0.050**	**-2.6**	**2.4**	**2.0**	**2.4**
1SE(median)	**0.357**	**0.273**	**1.038**	**0.501**	**0.381**	**0.022**	**0.137**	**0.222**	**0.143**	**0.091**	**0.127**	**0.101**	**0.069**	**0.062**	**0.086**	**0.263**	**0.116**	**0.116**	**0.002**	**0.0007**	**0.049**	**0.7**	**1.8**	**0.2**	**0.1**

Samples marked wih (*) were analyzed by S. G. in 2013 (Ginley, 2013). Internal error (%2SE) on 187Os/188Os estimated as ~±0.2% (Haller, 2017).
Samples marked wih (‡) were analyzed by M. H. in 2016 (Haller, 2017).
Samples marked with (†) were analyzed in 2019-2020 by V. A. F. (this study).
nd = not detected

Table 2. Summary of distinguishing characteristics of the mantle domain types identified in JOC harzburgites.								
	Subtype	**Possible protolith domain**	**Samples**	**Major elements**	**REE pattern**	**Eu/Eu* anomaly**	**Ir/Ir* anomaly**	**Pt/Pt* anomaly**
Type 1	LREE-depleted	abyssal	Grid 1, ATK76, ATK96	lower MgO	LREE-depleted planar	positive or negative	highly variable	frequently positive
	LREE-enriched	abyssal	Grid 2, JU15-23, ATK57(A-B), ATK75, ATK600	lower MgO	LREE-enriched planar to concave	often positive, some slightly negative	flat to slightly positive	positive to negative
Type 2	NA	SCLM	Grids 3, 4, ATK59, ATK589, JU15-1	higher MgO	sinusoidal with higher LREEs. Often La(N)<Ce(N)	strongly negative	flat to negative	frequently negative

Table 3. Median osmium isotopic compositions for a globally representative set of ophiolites.								
Locale	**Study**	**Age (Ga)**	**median γOs***	**1SE(median)**	**no. samples**			
Harzburgite/Peridotite								
Taitao Ophiolite, Chile	Schulte et al. (2009)	0.006	-2.9	0.8	18			
New Caledonia, Oceania	Secchiari et al., (2020)	0.053	-1.3	1.3	4			
Mugla Ophiolite, Turkey	Uysal et al. (2012)	0.065	-1.3	0.9	9			
Troodos Ophiolite, Cyprus	Büchl et al. (2002)	0.09	2.1	0.7	3			
Western YZO (Purang), Yarlung-Zangbo Opholite, Tibet	Xu et al. (2020)	0.13	-0.9	1.4	17			
Coast Range, California, USA	Snortum and Day (2020)	0.161	2.0	0.9	3			
Mamonia Complex, Cyprus	Batanova et al. (2008)	0.2	0.4	NA	1			
Ligurian Ophiolites	Snow et al. (2000)	0.18	0.4	0.1	18			
Shetland Ophiolite Complex, Scotland	O'Driscoll et al. (2012)	0.492	0.7	0.7	21			
Leka Ophiolite, Norway	O'Driscoll et al. (2015); Haller et al. (2021)	0.497	0.0	0.4	41			
Gangou Ophiolite, Tianshan ophiolites, NW China	Gong et al. (2020)	0.516	-3.2	2.1	4			
Eastern Alps, Austria	Melcher and Meisel (2004)	0.55	-0.3	1.6	4			
Jormua Ophiolite Complex	This study	1.95	-2.0	0.9	17			
Dongwanzi Ophiolite (peridotites only)**	Kusky et al. (2007)	2.5	0.3	0.3	4			
Chromites								
Tiebaghi, New Caledonia	Walker et al. (2002)	0.05	0.9	NA	1			
St. Elena, Costa Rica	Walker et al. (2002)	0.08	0.1	0.8	2			
Mayari-Baracoa Ophiolite	Frei et al. (2006)	0.09	-2.2	0.3	17			
Troodos, Cyprus	Walker et al. (2002)	0.091	1.3	0.4	4			
Semail, Oman	Walker et al. (2002)	0.096	3.1	1.2	5			
Elistratova Ophiolite, Russia	Walker et al. (2002)	0.1	-0.7	NA	1			
Bulquiza, Albania	Walker et al. (2002)	0.155	-0.4	NA	1			
Kukes-Kalamash, Albania	Walker et al. (2002)	0.155	0.9	NA	1			
Horokanai, Japan	Walker et al. (2002)	0.16	-0.6	0.7	4			
Luobasa and Dongqiao, Tibet (Type I)	Shi et al. (2007)	0.196	0.5	0.1	16			
Luobasa and Dongqiao, Tibet (Type II)	Shi et al. (2007)	0.196	-3.7	0.3	7			
Dun Mtn., New Zealand	Walker et al. (2002)	0.27	5.4	NA	1			
Yakuno, Japan	Walker et al. (2002)	0.28	0.6	0.1	3			
La Cabaña ultramafic bodies, central Chile	Gonzáles-Jiménez et al. (2014)	0.3	1.4	0.5	4			
Kempirsai, Urals, Russia	Walker et al. (2002)	0.4	-0.2	0.2	3			
Oeyama, Japan	Walker et al. (2002)	0.42	0.5	0.1	2			
Ray Iz, Polar Urals, Russia	Walker et al. (2002)	0.47	1.5	0.7	3			
Unst, Shetland Islands, Scotland	Walker et al. (2002)	0.473	1.1	NA	1			
Leka, Norway	Walker et al. (2002)	0.497	2.5	1.0	3			
Al' Ays, Saudi Arabia	Walker et al. (2002)	0.75	0.7	1.3	5			
Morro Feio, Brazil	Walker et al. (2002)	0.9	2.9	NA	1			
Cromínia, Brazil	Walker et al. (2002)	0.9	2.9	0.5	2			
*Datasets were filtered to exclude samples with high 187Re/188Os (>0.25; Tsuru et al., 2000). γOs was recalculated for each locale, using the same approach as for the JOC data in Table 1.								
**The status of Dongwanzi as an Archean ophiolite complex has been the subject of debate (Kusky et al., 2001; 2002; 2007; Zhai et al., 2002; Zhao et al., 2007). We include it here for thoroughness.								

Figure 1

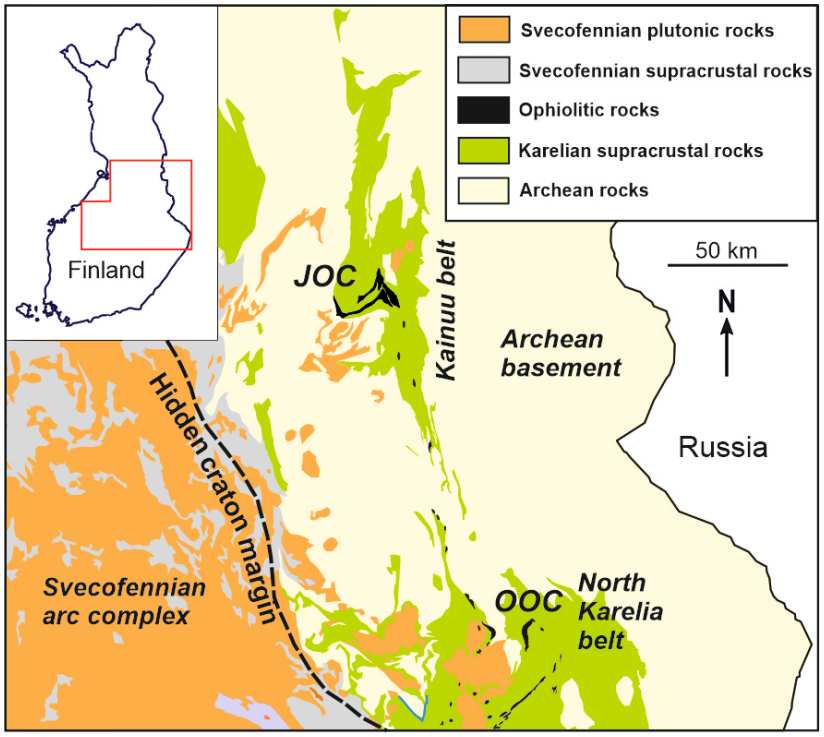
Svecofennian plutonic rocks
Svecofennian supracrustal rocks
Ophiolitic rocks
Karelian supracrustal rocks
Archean rocks
Finland
JOC
Kainuu belt
Archean basement
50 km
N
Russia
Hidden craton margin
Svecofennian arc complex
OOC
North Karelia belt

Figure 2

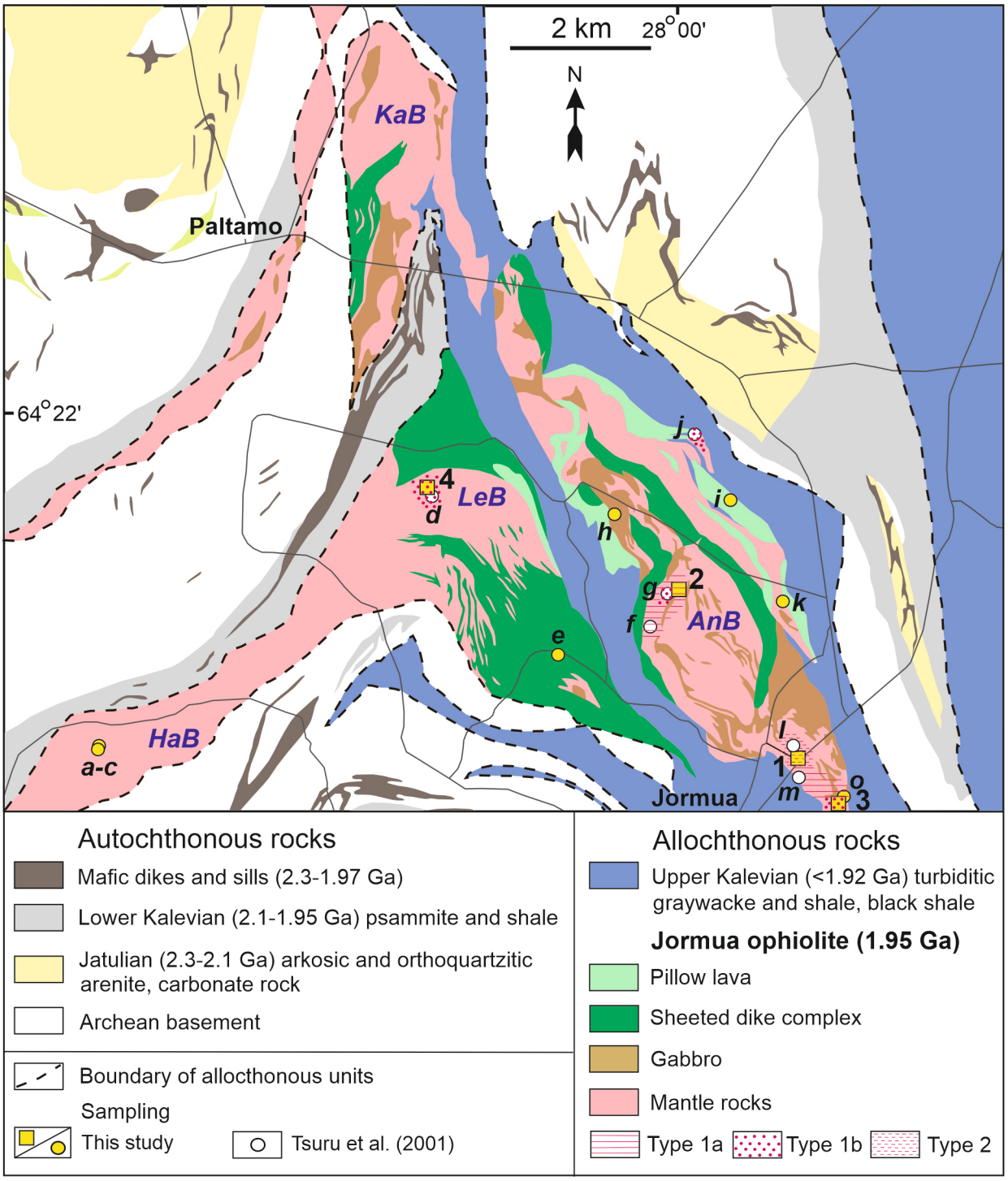
2 km
28°00'
N
KaB
Paltamo
64°22'
LeB
AnB
HaB
Jormua
a-c
d
e
f
g
h
i
j
k
l
m
1
2
3
4
Autochthonous rocks
Mafic dikes and sills (2.3-1.97 Ga)
Lower Kalevian (2.1-1.95 Ga) psammite and shale
Jatulian (2.3-2.1 Ga) arkosic and orthoquartzitic arenite, carbonate rock
Archean basement
Boundary of allocthonous units
Sampling
This study
Tsuru et al. (2001)
Allochthonous rocks
Upper Kalevian (<1.92 Ga) turbiditic graywacke and shale, black shale
Jormua ophiolite (1.95 Ga)
Pillow lava
Sheeted dike complex
Gabbro
Mantle rocks
Type 1a
Type 1b
Type 2

Figure 3 - field photos

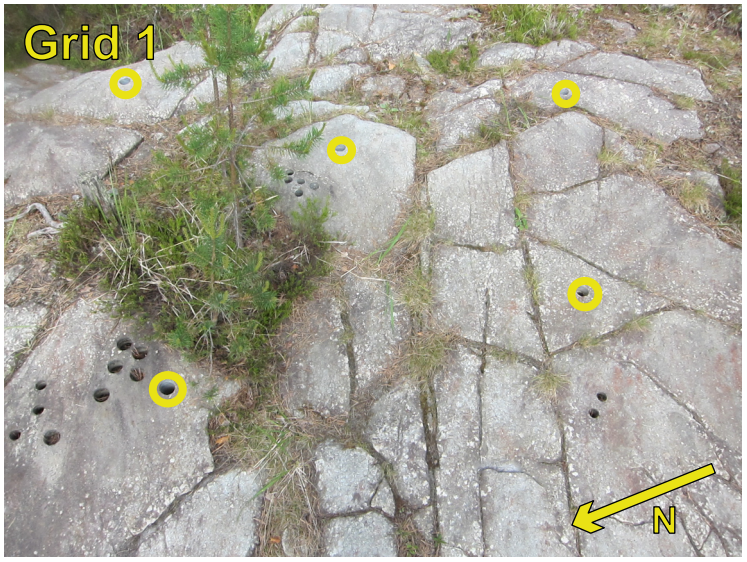

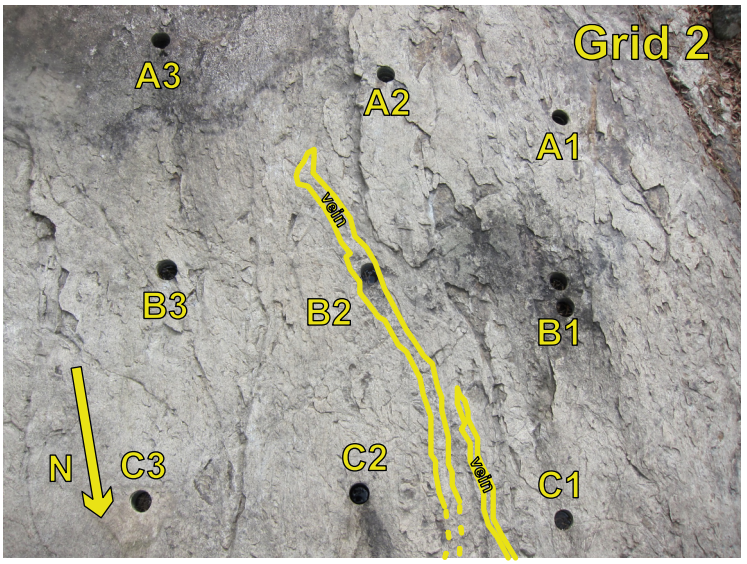

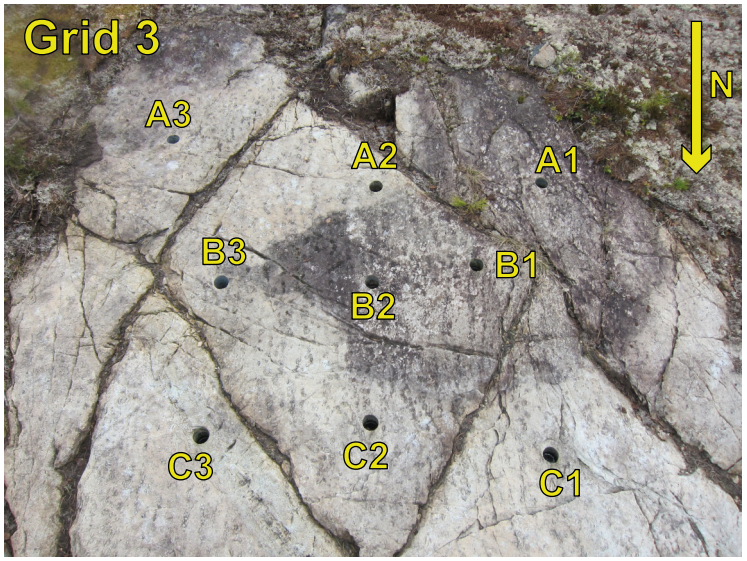

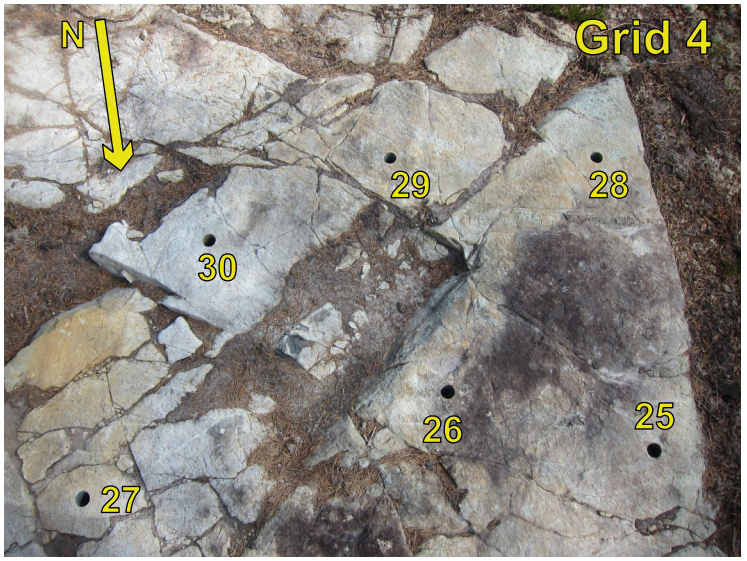

Figure 4

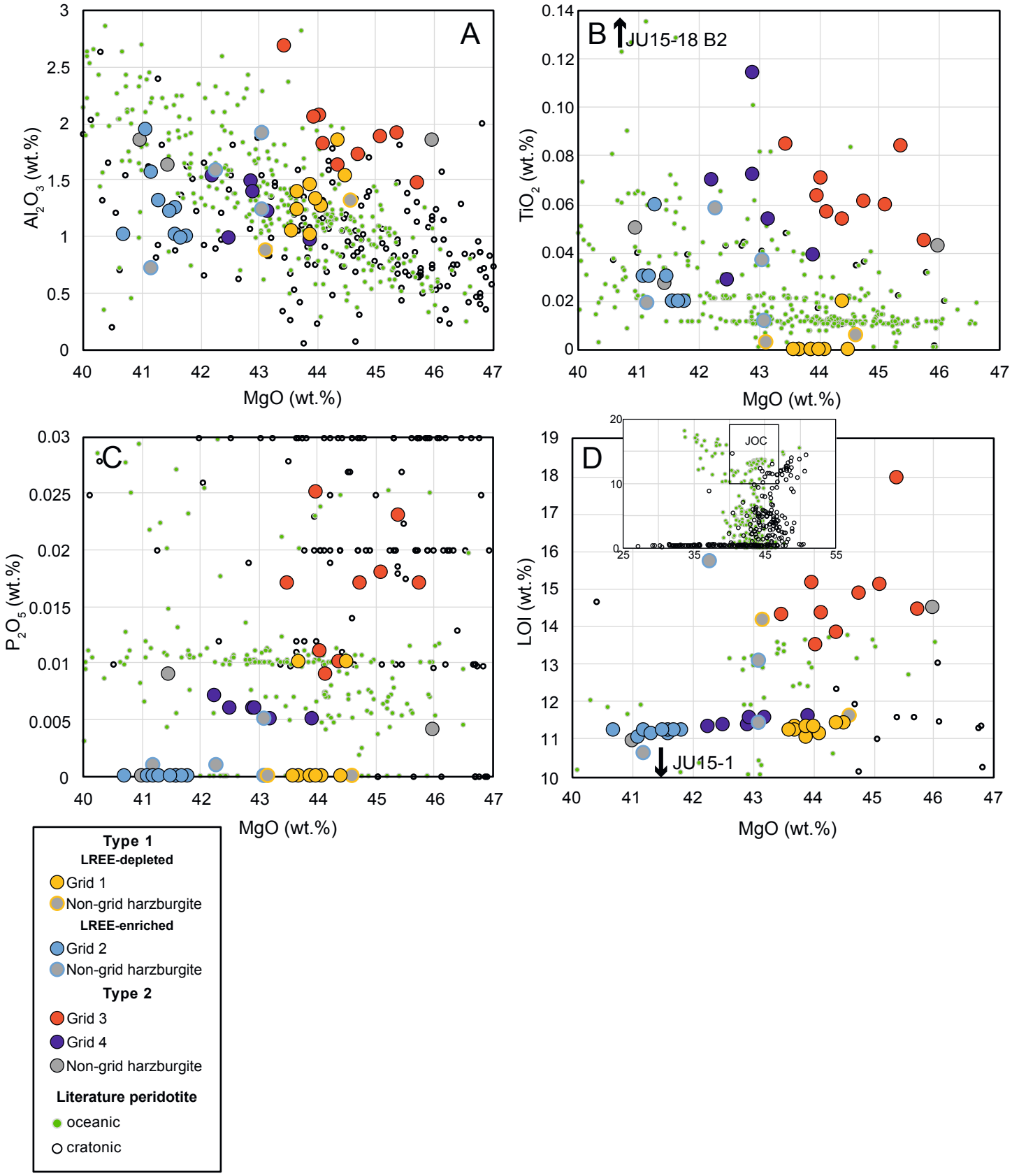
A
B
JU15-18 B2
C
D
JOC
JU15-1
MgO (wt.%)
Al2O3 (wt.%)
TiO2 (wt.%)
P2O5 (wt.%)
LOI (wt.%)
Type 1
LREE-depleted
Grid 1
Non-grid harzburgite
LREE-enriched
Grid 2
Non-grid harzburgite
Type 2
Grid 3
Grid 4
Non-grid harzburgite
Literature peridotite
oceanic
cratonic

Figure 5

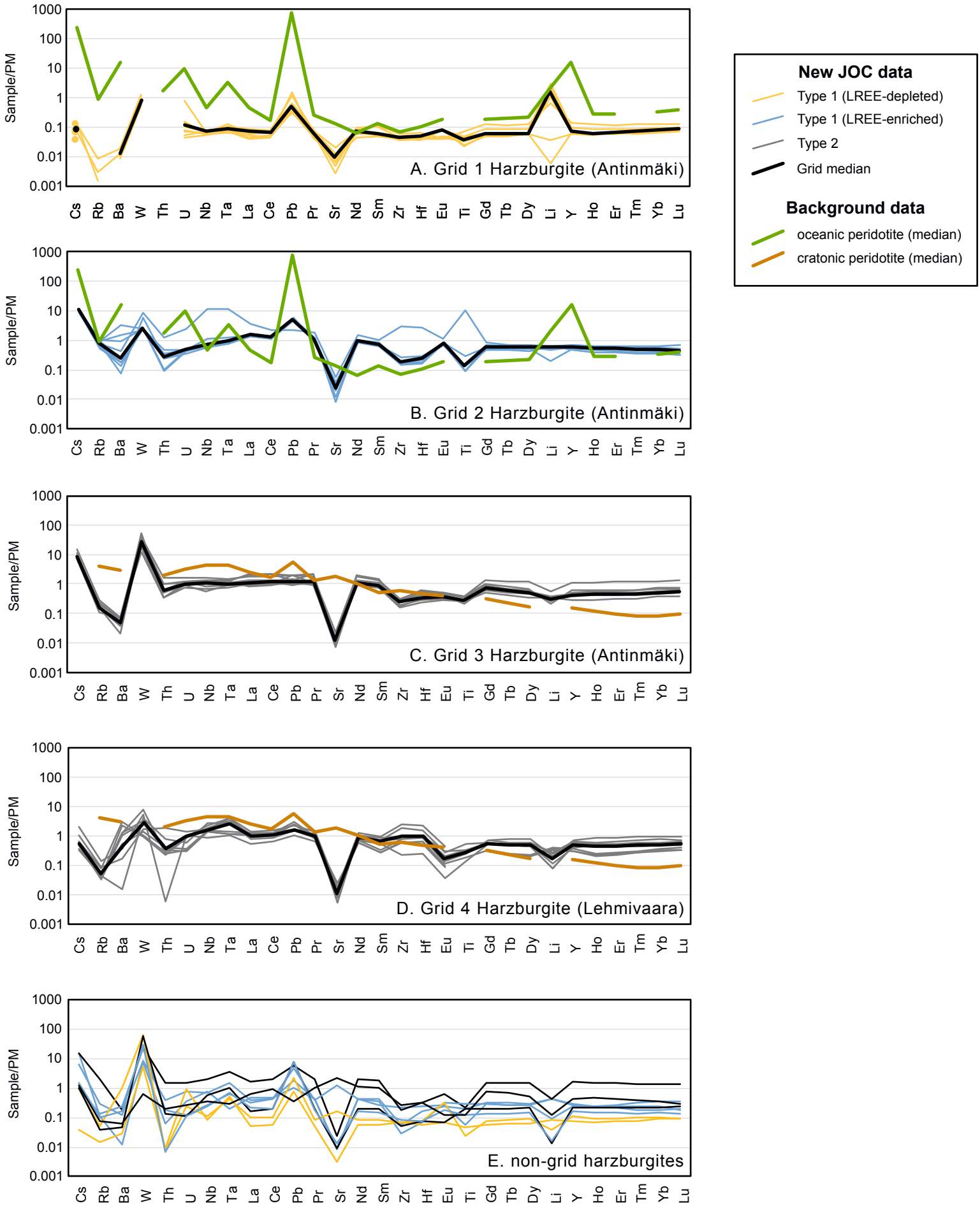
Sample/PM
1000
100
10
1
0.1
0.01
0.001
Cs Rb Ba W Th U Nb Ta La Ce Pb Pr Sr Nd Sm Zr Hf Eu Ti Gd Tb Dy Li Y Ho Er Tm Yb Lu
A. Grid 1 Harzburgite (Antinmäki)
B. Grid 2 Harzburgite (Antinmäki)
C. Grid 3 Harzburgite (Antinmäki)
D. Grid 4 Harzburgite (Lehmivaara)
E. non-grid harzburgites
New JOC data
Type 1 (LREE-depleted)
Type 1 (LREE-enriched)
Type 2
Grid median
Background data
oceanic peridotite (median)
cratonic peridotite (median)

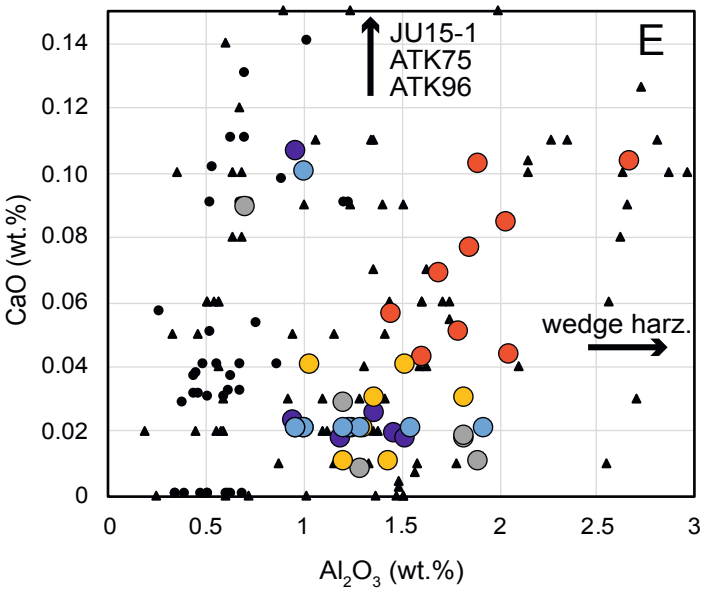
E
JU15-1
ATK75
ATK96
wedge harz.
CaO (wt.%)
Al_2O_3 (wt.%)
0.14
0.12
0.10
0.08
0.06
0.04
0.02
0
0
0.5
1
1.5
2
2.5
3

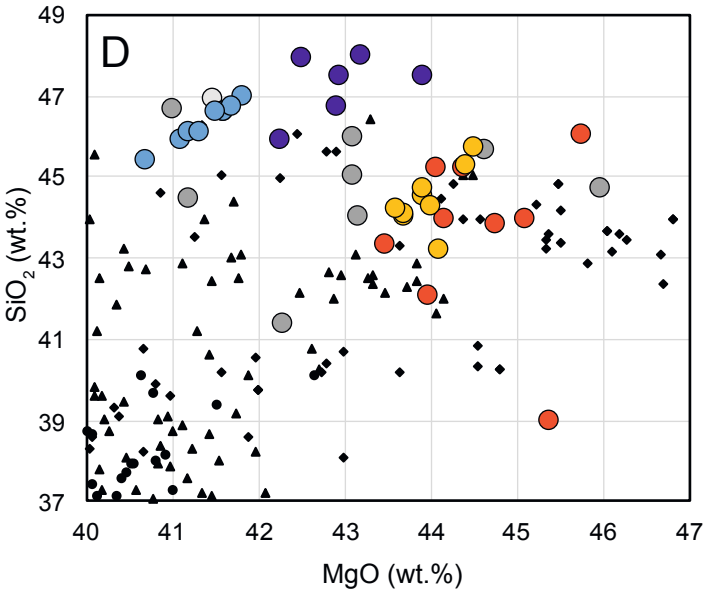
D
SiO_2 (wt.%)
MgO (wt.%)
49
47
45
43
41
39
37
40
41
42
43
44
45
46
47

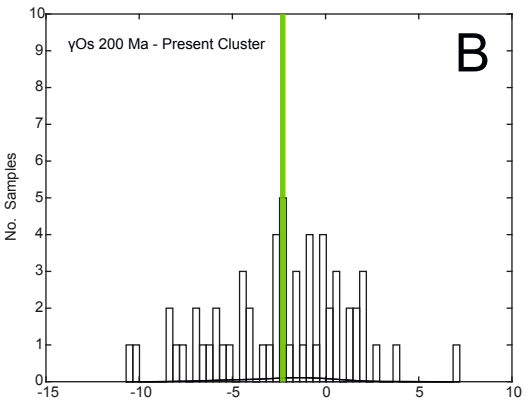
B
γOs 200 Ma - Present Cluster
No. Samples
10
9
8
7
6
5
4
3
2
1
0
-15
-10
-5
0
5
10

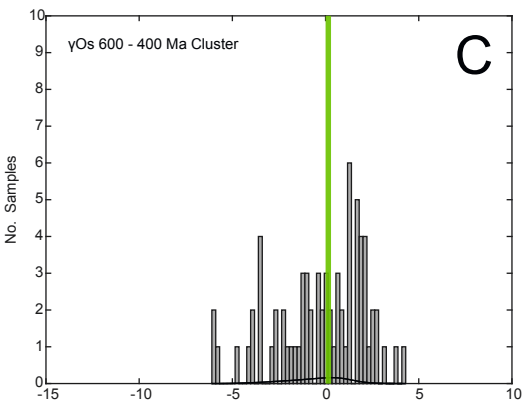
C
γOs 600 - 400 Ma Cluster
No. Samples
10
9
8
7
6
5
4
3
2
1
0
-15
-10
-5
0
5
10

Figure 6

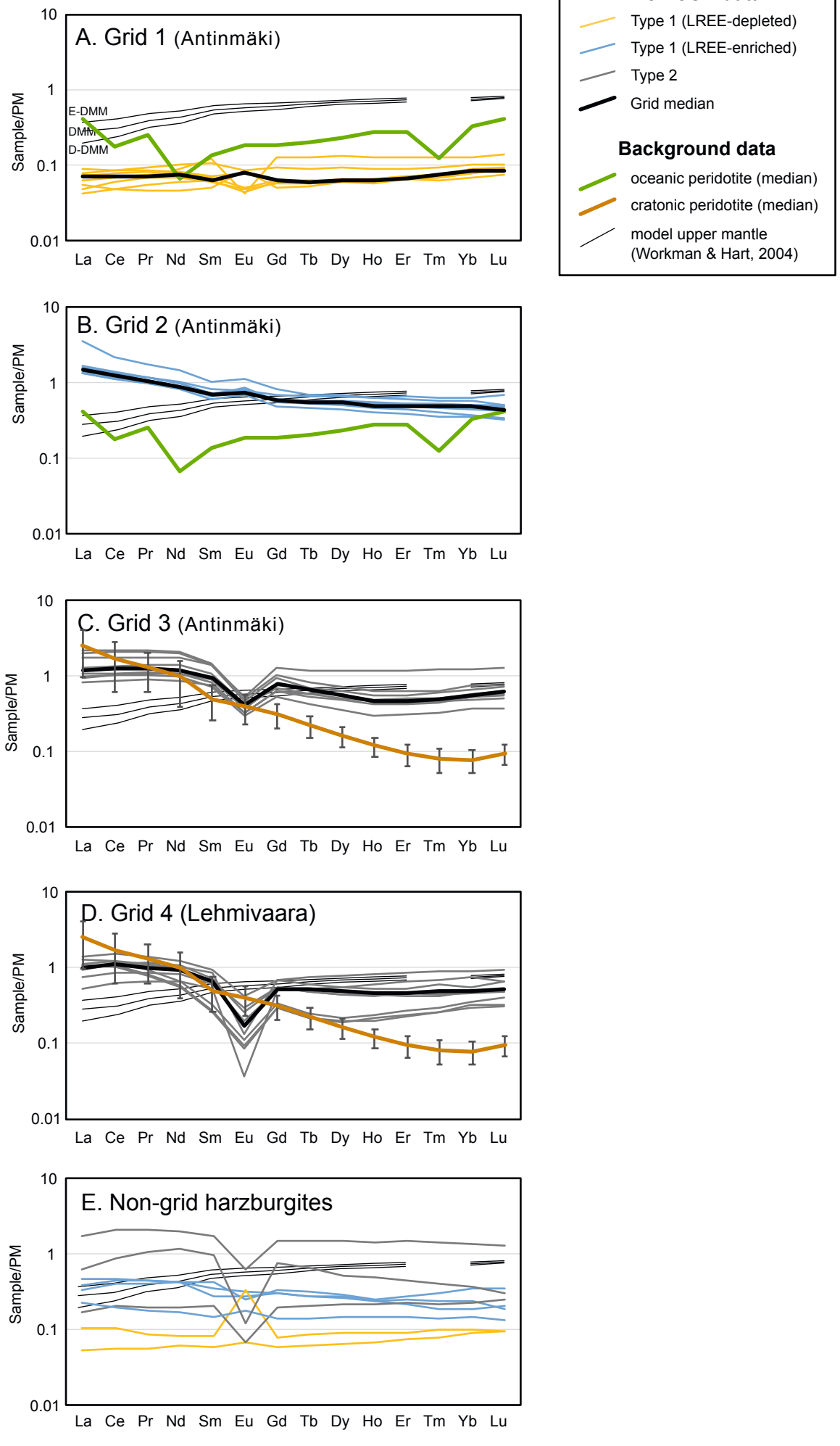
A. Grid 1 (Antinmäki)
B. Grid 2 (Antinmäki)
C. Grid 3 (Antinmäki)
D. Grid 4 (Lehmivaara)
E. Non-grid harzburgites
Sample/PM
10
1
0.1
0.01
E-DMM
DMM
D-DMM
La Ce Pr Nd Sm Eu Gd Tb Dy Ho Er Tm Yb Lu
New JOC data
Type 1 (LREE-depleted)
Type 1 (LREE-enriched)
Type 2
Grid median
Background data
oceanic peridotite (median)
cratonic peridotite (median)
model upper mantle
(Workman & Hart, 2004)

Figure 7

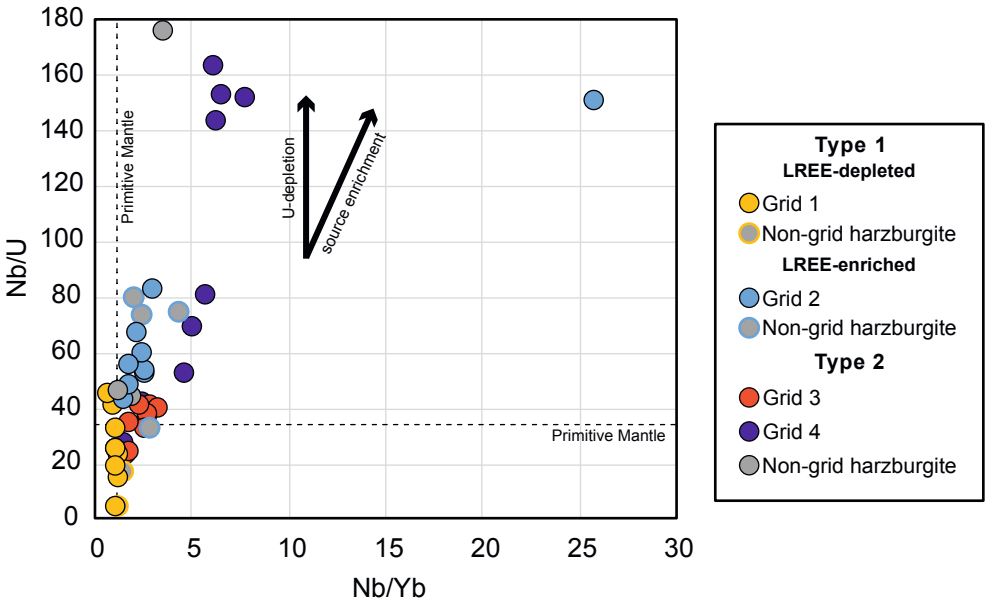
Nb/U
Nb/Yb
0
20
40
60
80
100
120
140
160
180
0
5
10
15
20
25
30
Primitive Mantle
Primitive Mantle
U-depletion
source enrichment
Type 1
LREE-depleted
Grid 1
Non-grid harzburgite
LREE-enriched
Grid 2
Non-grid harzburgite
Type 2
Grid 3
Grid 4
Non-grid harzburgite

Figure 8

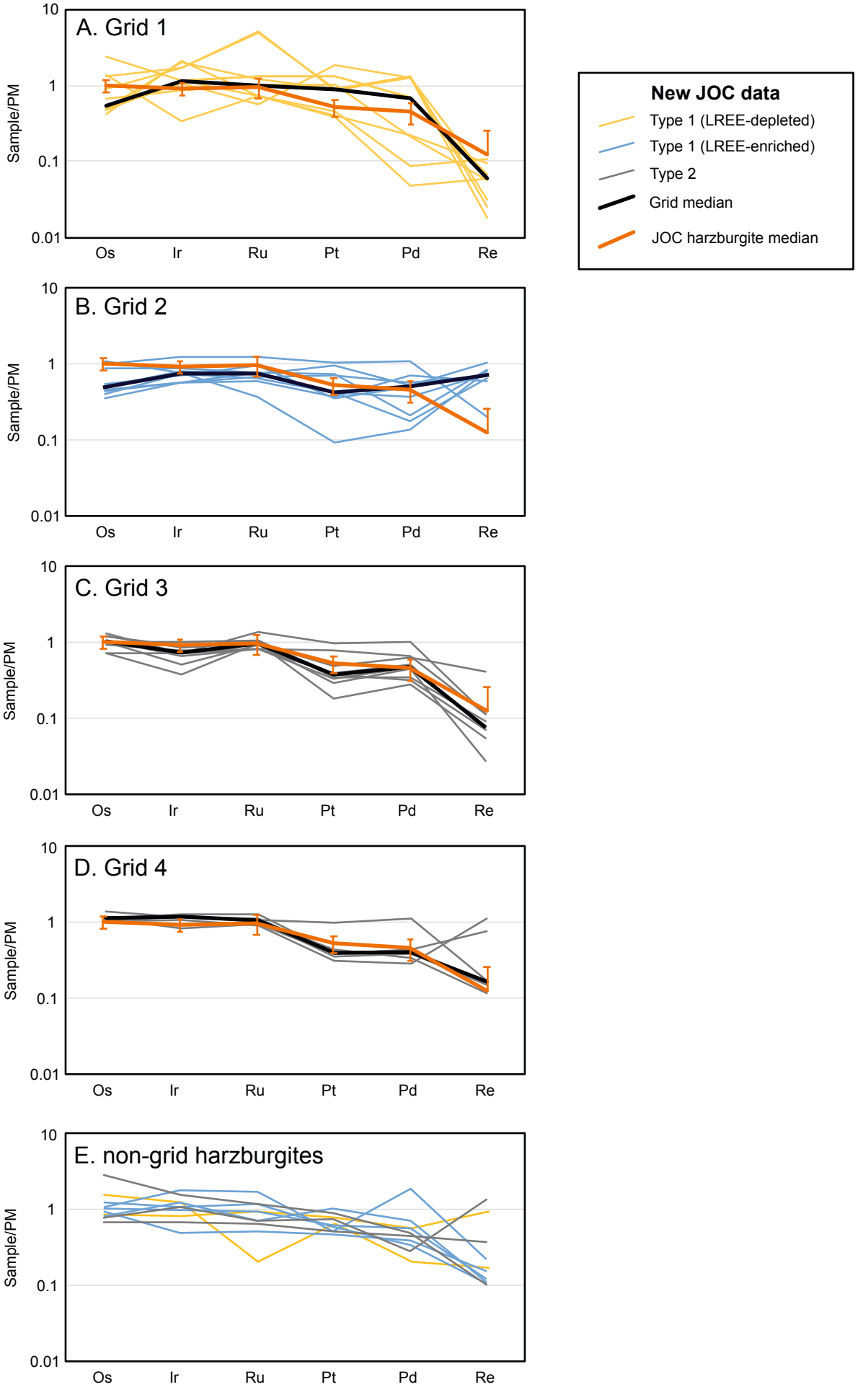
A. Grid 1
B. Grid 2
C. Grid 3
D. Grid 4
E. non-grid harzburgites
Sample/PM
10
1
0.1
0.01
Os
Ir
Ru
Pt
Pd
Re
New JOC data
Type 1 (LREE-depleted)
Type 1 (LREE-enriched)
Type 2
Grid median
JOC harzburgite median

Figure 9

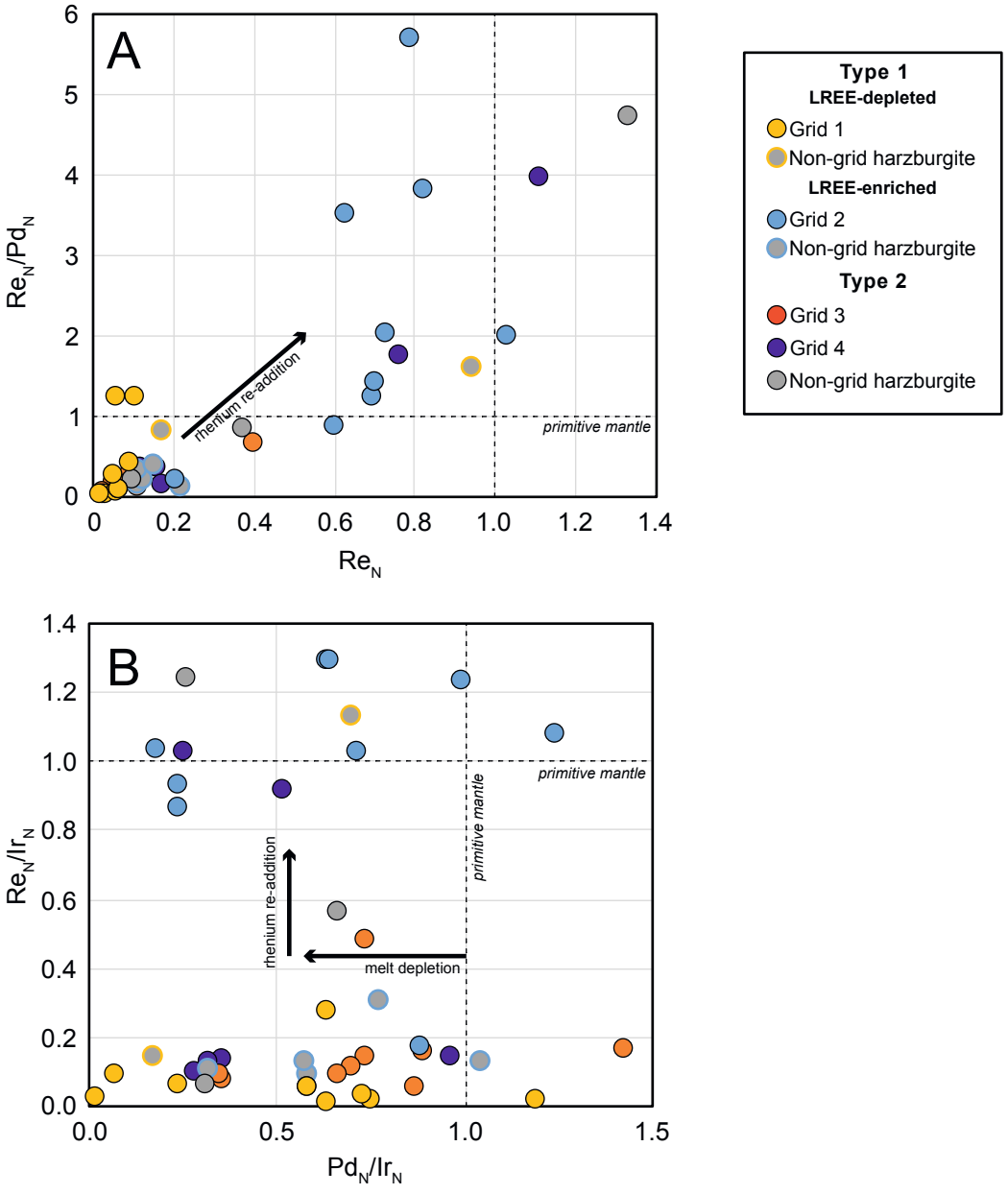
A
B
Type 1
LREE-depleted
Grid 1
Non-grid harzburgite
LREE-enriched
Grid 2
Non-grid harzburgite
Type 2
Grid 3
Grid 4
Non-grid harzburgite
rhenium re-addition
primitive mantle
melt depletion
Re_N/Pd_N
Re_N
Re_N/Ir_N
Pd_N/Ir_N

Figure 10

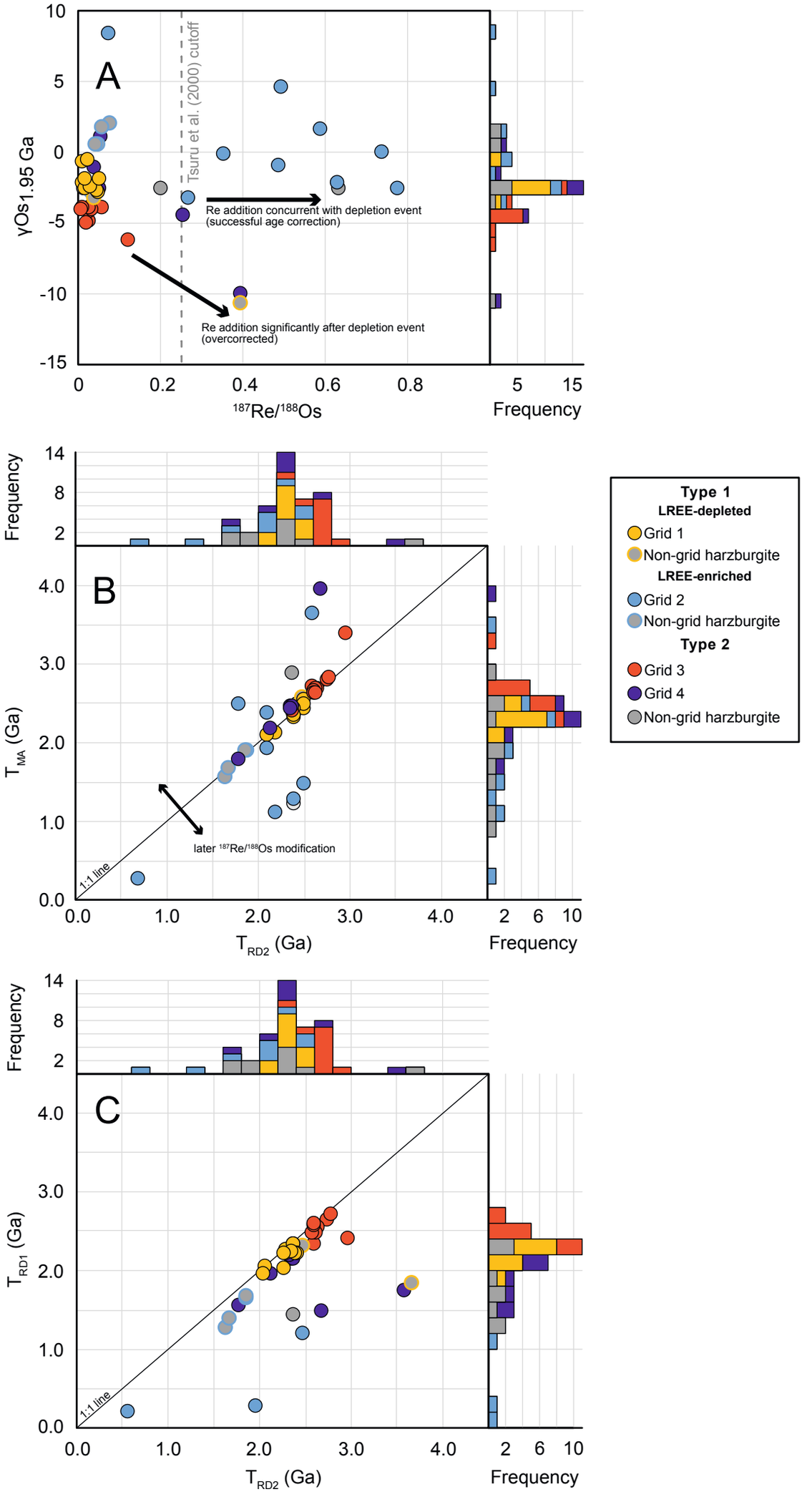
A
γOs1.95 Ga
Tsuru et al. (2000) cutoff
Re addition concurrent with depletion event
(successful age correction)
Re addition significantly after depletion event
(overcorrected)
187Re/188Os
Frequency
B
Frequency
TMA (Ga)
later 187Re/188Os modification
1:1 line
TRD2 (Ga)
Frequency
C
Frequency
TRD1 (Ga)
1:1 line
TRD2 (Ga)
Frequency
Type 1
LREE-depleted
Grid 1
Non-grid harzburgite
LREE-enriched
Grid 2
Non-grid harzburgite
Type 2
Grid 3
Grid 4
Non-grid harzburgite

Figure 11

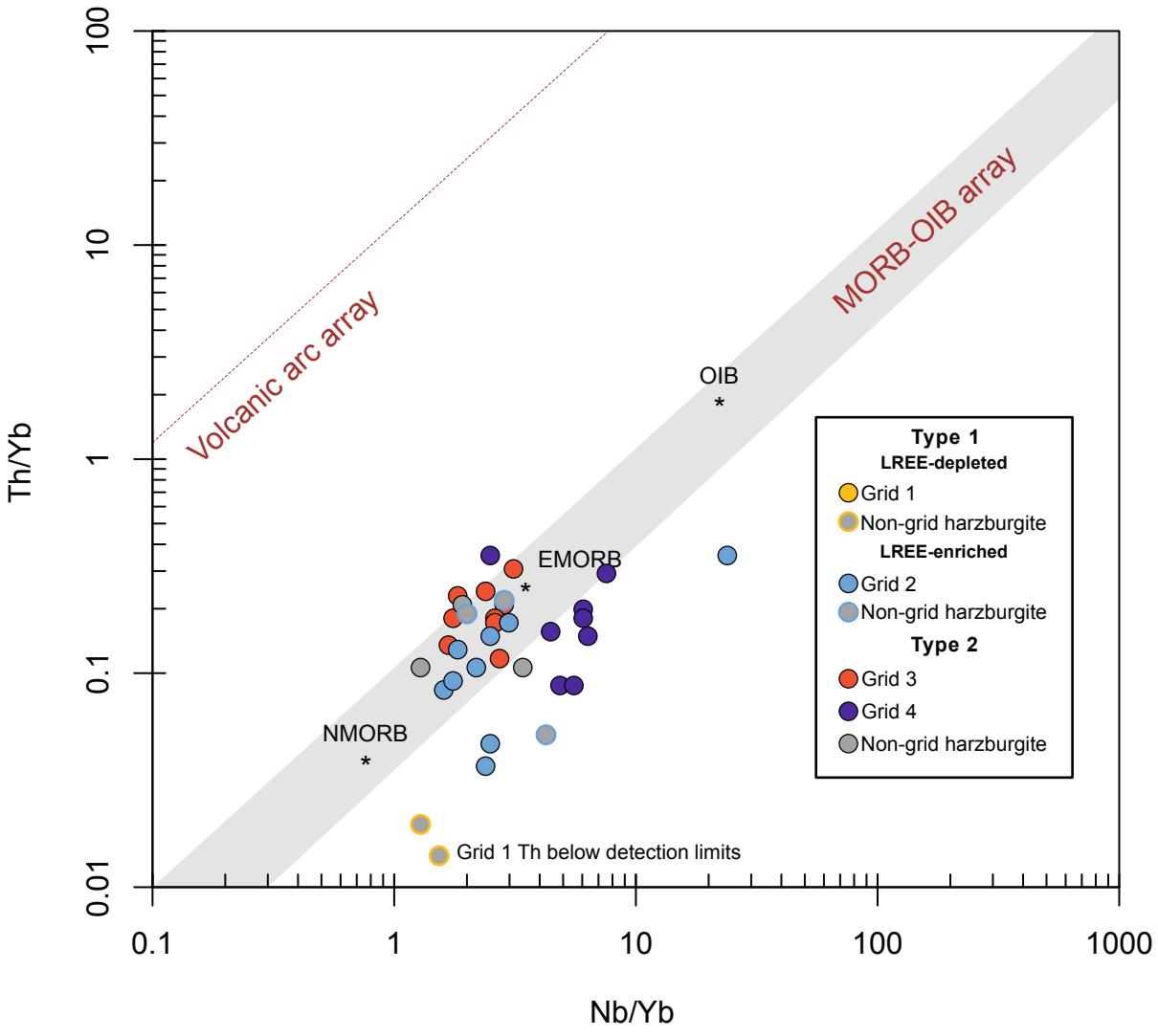
Th/Yb
Nb/Yb
100
10
1
0.1
0.01
0.1
1
10
100
1000
Volcanic arc array
MORB-OIB array
OIB
EMORB
NMORB
Grid 1 Th below detection limits
Type 1
LREE-depleted
Grid 1
Non-grid harzburgite
LREE-enriched
Grid 2
Non-grid harzburgite
Type 2
Grid 3
Grid 4
Non-grid harzburgite

Figure 12

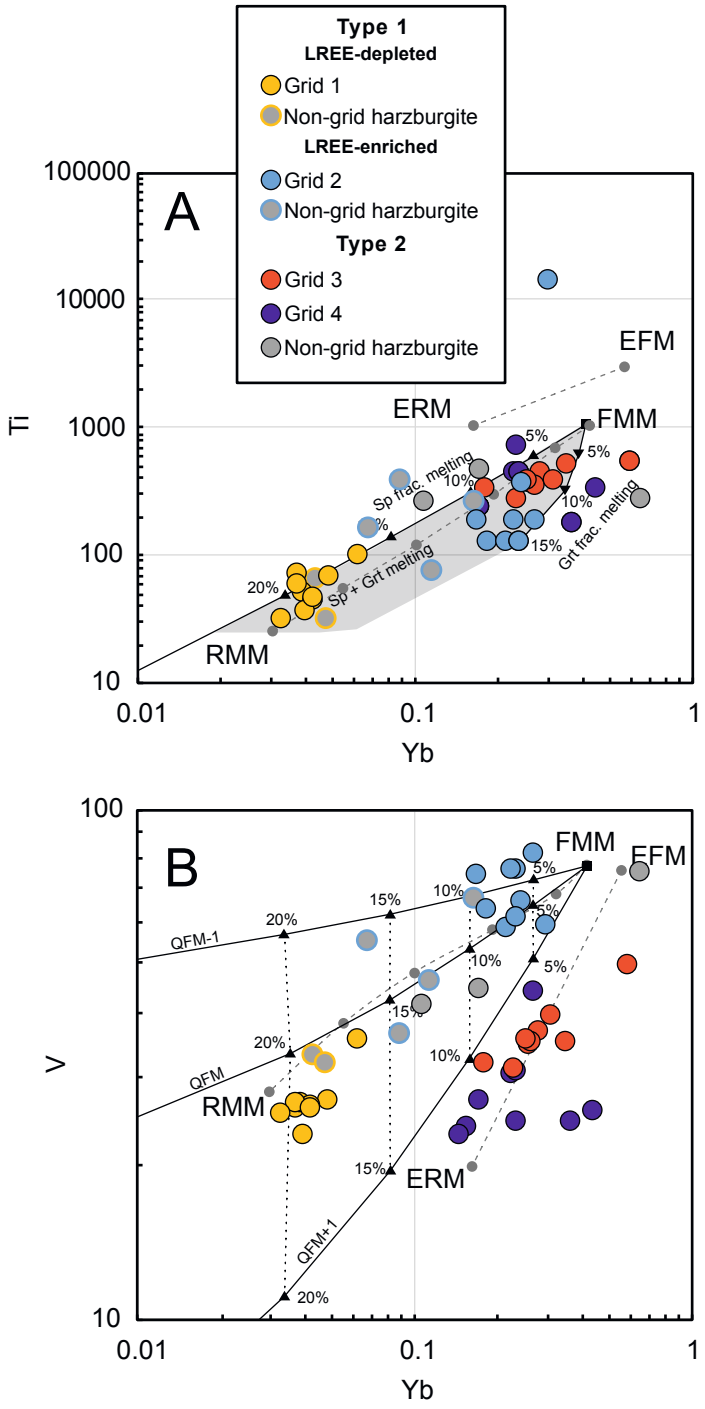
Type 1
LREE-depleted
Grid 1
Non-grid harzburgite
LREE-enriched
Grid 2
Non-grid harzburgite
Type 2
Grid 3
Grid 4
Non-grid harzburgite
A
Ti
100000
10000
1000
100
10
0.01
0.1
1
Yb
EFM
ERM
FMM
RMM
Sp frac. melting
Sp + Grt melting
Grt frac. melting
5%
10%
15%
20%
B
V
100
10
0.01
0.1
1
Yb
FMM
EFM
ERM
RMM
QFM-1
QFM
QFM+1
5%
10%
15%
20%

Figure 13

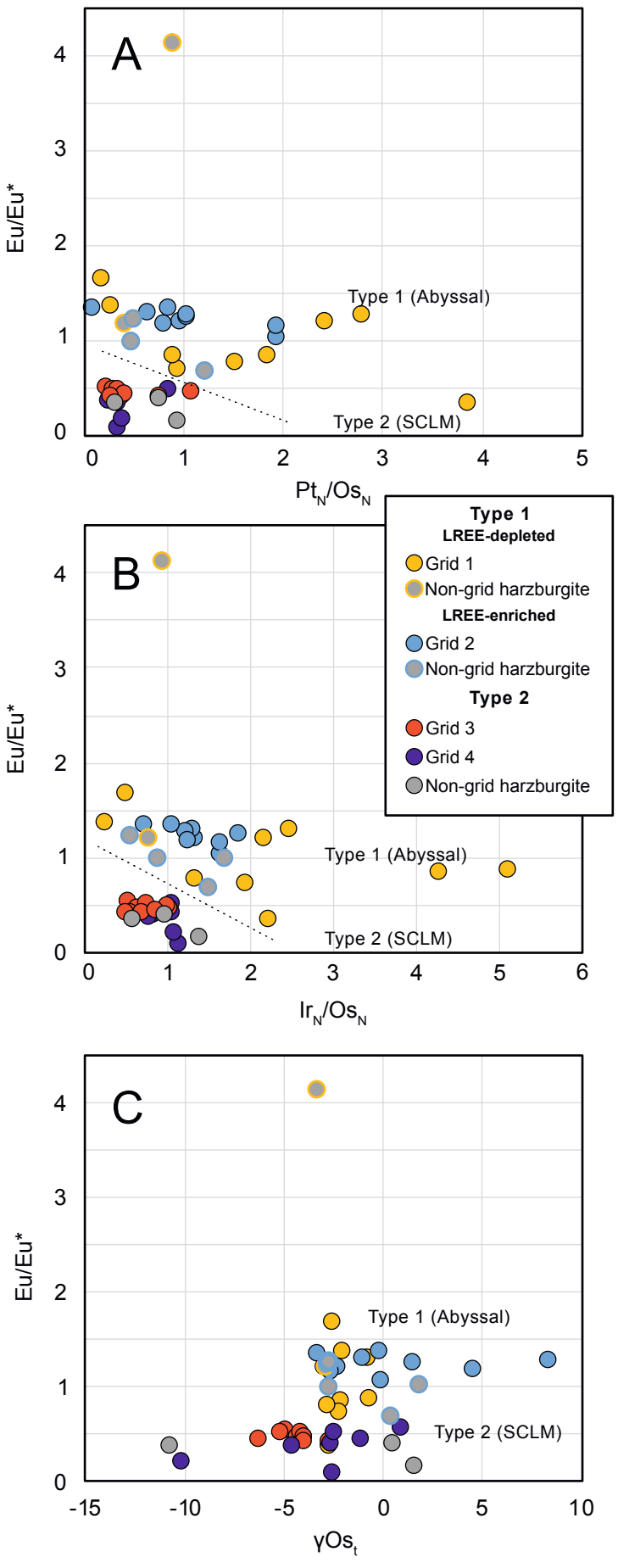
A
B
C
Eu/Eu*
Pt_N/Os_N
Ir_N/Os_N
γOs_t
Type 1 (Abyssal)
Type 2 (SCLM)
Type 1
LREE-depleted
Grid 1
Non-grid harzburgite
LREE-enriched
Grid 2
Non-grid harzburgite
Type 2
Grid 3
Grid 4
Non-grid harzburgite

Figure 14

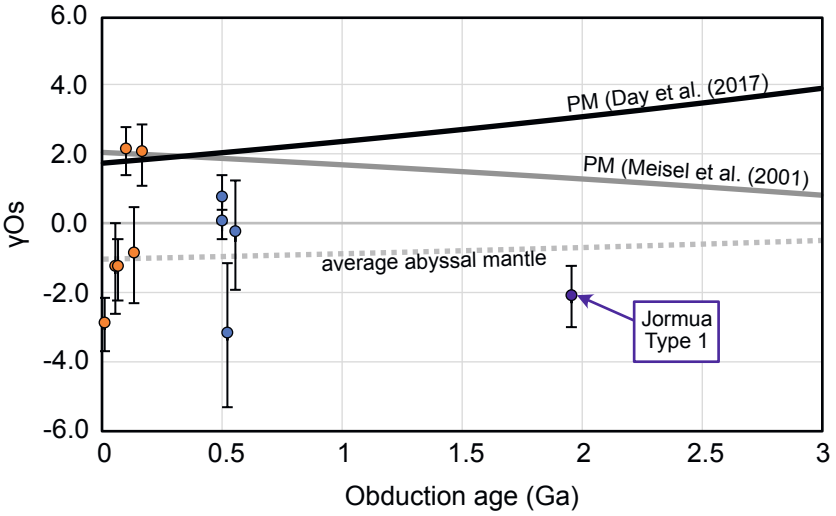
6.0
4.0
2.0
0.0
-2.0
-4.0
-6.0
yOs
0
0.5
1
1.5
2
2.5
3
Obduction age (Ga)
PM (Day et al. (2017)
PM (Meisel et al. (2001)
average abyssal mantle
Jormua
Type 1